Matter and Radiation at Extremes | RESEARCH ARTICLE | scitation.org/journal/mre

Current status and highlights of the ELI-NP research program

Cite as: Matter Radiat. Extremes 5, 024402 (2020); doi: 10.1063/1.5093535
Submitted: 6 June 2019 • Accepted: 9 February 2020 •
Published Online: 13 March 2020

K. A. Tanaka,[1,a)] K. M. Spohr,[1] D. L. Balabanski,[1] S. Balascuta,[1] L. Capponi,[1] M. O. Cernaianu,[1] M. Cuciuc,[1] A. Cucoanes,[1] I. Dancus,[1] A. Dhal,[1] B. Diaconescu,[1] D. Doria,[1] P. Ghenuche,[1] D. G. Ghita,[1] S. Kisyov,[1] V. Nastasa,[1] J. F. Ong,[1] F. Rotaru,[1] D. Sangwan,[1] P.-A. Söderström,[1] D. Stutman,[1,2] G. Suliman,[1] O. Tesileanu,[1] L. Tudor,[1] N. Tsoneva,[1] C. A. Ur,[1] D. Ursescu,[1] and N. V. Zamfir[1]

AFFILIATIONS

[1] Extreme Light Infrastructure (ELI-NP) and Horia Hulubei National Institute for R & D in Physics and Nuclear Engineering (IFIN-HH), Str. Reactorului No. 30, 077125 Bucharest–Măgurele, Romania

[2] Johns Hopkins University, 3400 N. Charles Street, Baltimore, Maryland 21218, USA

[a)] **Author to whom correspondence should be addressed:** kazuo.tanaka@eli-np.ro

ABSTRACT

The emergence of a new era reaching beyond current state-of-the-art ultrashort and ultraintense laser technology has been enabled by the approval of around € 850 million worth of structural funds in 2011–2012 by the European Commission for the installation of Extreme Light Infrastructure (ELI). The ELI project consists of three pillars being built in the Czech Republic, Hungary, and Romania. This challenging proposal is based on recent technical progress allowing ultraintense laser fields in which intensities will soon be reaching as high as $I_0 \sim 10^{23}$ W cm^{-2}. This tremendous technological advance has been brought about by the invention of chirped pulse amplification by Mourou and Strickland. Romania is hosting the ELI for Nuclear Physics (ELI-NP) pillar in Măgurele near Bucharest. The new facility, currently under construction, is intended to serve the broad national, European, and international scientific community. Its mission covers scientific research at the frontier of knowledge involving two domains. The first is laser-driven experiments related to NP, strong-field quantum electrodynamics, and associated vacuum effects. The second research domain is based on the establishment of a Compton-backscattering-based, high-brilliance, and intense γ beam with $E_\gamma \lesssim 19.5$ MeV, which represents a merger between laser and accelerator technology. This system will allow the investigation of the nuclear structure of selected isotopes and nuclear reactions of relevance, for example, to astrophysics with hitherto unprecedented resolution and accuracy. In addition to fundamental themes, a large number of applications with significant societal impact will be developed. The implementation of the project started in January 2013 and is spearheaded by the ELI-NP/Horia Hulubei National Institute for Physics and Nuclear Engineering (IFIN-HH). Experiments will begin in early 2020.

I. INTRODUCTION

The era of modern-day high-power laser systems was instigated by the groundbreaking technological breakthrough of chirped pulse amplification (CPA) developed in 1986 by Strickland and Mourou,[1] who were honored with the 2018 Nobel Prize in Physics for this work. At the Extreme Light Infrastructure for Nuclear Physics (ELI-NP) laboratory, facilities that are capable of supplying the highest focused laser intensity I_0 are currently being implemented, characterized by light pulses in the petawatt (PW) regime lasting for tens of femtoseconds. Exploiting these highest human-made intensities, particles and γ photons will be produced that are characterized by hitherto unreachable quality parameters with regard to, for example, coherence, brilliance, and spectral features relating to the energy and time distributions of the induced radiations.[2–6] Such intense beams are relevant to nuclear physics, allowing the exploration of new regimes, thus extending research based on traditional accelerator technology. ELI-NP aims to provide a flagship installation of a high-power laser system (HPLS) for the scientific community worldwide. The HPLS will consist of two independent laser arm segments, each providing a maximum power of 10 PW (10^{16} W).

Also, a high-brilliance and high-intensity γ beamline called the Variable-Energy Gamma Ray (VEGA) system, which takes advantage of the Compton backscattering process, will be installed. At the HPLS, the acceleration of electrons to many tens of GeV within centimeter distances will be tested. Such high electron energies are currently only supplied by large RF-based accelerator systems. Secondary nuclear fission or fusion reactions on specific materials will also be investigated with the use of high-density beam bunches of energetic protons and heavier ions, potentially leading to the efficient production of medical radioisotopes and to improvements in nuclear-related diagnostic tools. Multistep reactions, such as fission–fusion, will be probed to address questions regarding the formation of the heaviest elements in the universe under stellar conditions. Furthermore, a new scheme of high-contrast X-ray imaging may be achievable for high-resolution medical observation. The HPLS at ELI-NP will also allow the study of how matter/antimatter may be produced out of pure vacuum by intense radiation fields. Moreover, materials and biological samples can be subjected to intense radiation fields to inform, for example, space mission applications.

The newly developed VEGA system at ELI-NP will be used to study key nuclear reactions relevant to nucleosynthesis, such as the fusion of α particles and carbon nuclei to produce oxygen ($^{4}\mathrm{He} + {}^{12}\mathrm{C} \rightarrow {}^{16}\mathrm{O}$), which lies at the root of life on Earth. Furthermore, nuclear resonance fluorescence (NRF) measurements with the highest resolution can be undertaken with the intense, tunable beam of γ radiation of up to E_γ = 19.5 MeV. NRF-based novel technologies can also lead to a manifold of applications, for example, within imaging and γ tomography, potentially enhancing the field of nuclear security. In the following sections, descriptions of the two core facilities at ELI-NP, namely, the HPLS and the VEGA system, are given. The status of implementation of the ELI-NP facilities currently under construction is summarized. Concise technical descriptions are provided, together with some selected, high-priority, physics projects planned with the multi-PW lasers and the multi-MeV brilliant γ beam. Furthermore, some selected inaugural commissioning campaigns and newly developed instrumentation are discussed.

II. STATUS OF THE ELI-NP FACILITY 2018/19

A. Overview of the HPLS and the VEGA system at ELI-NP

The HPLS was designed to serve the scientific cases suggested in the ELI-Whitebook published in 2010, thus pushing the boundaries of high-intensity laser-plasma research worldwide.[7] To enable such research, the HPLS beams will be routed under vacuum to large custom-made experimental chambers in dedicated experimental target areas. A total of nine target areas named E1 to E9 are currently built. The laser system was installed by the Thales Group, a world-leading provider of state-of-the-art laser technology based in Paris and Romania. Final tests of the HPLS are being undertaken as of December 2019. The HPLS consists of three separated high-power

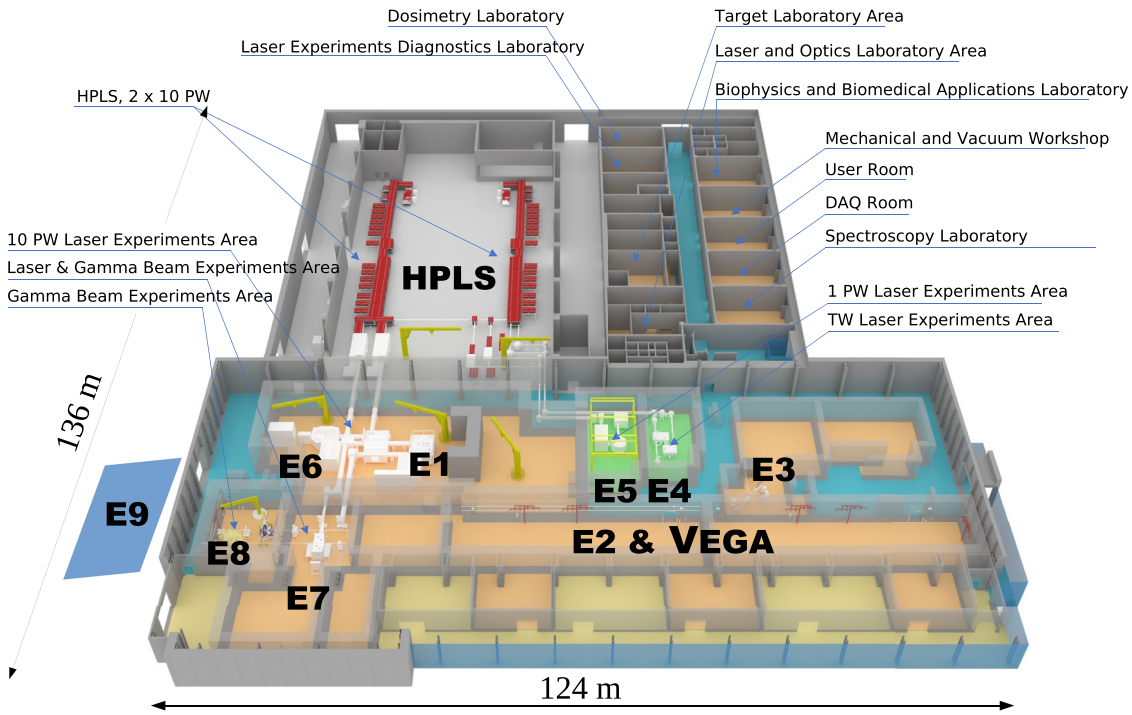

FIG. 1. Schematic overview of the HPLS and the VEGA system and associated target areas at ELI-NP. The two laser arms are depicted in red. The target areas E1, E4, E5, E6, and E7 show the 3D CAD designs of the target chambers currently under construction. The positions of the target areas E3, E8, and E9 associated with the VEGA system are indicated. The E9 area sits in the newly installed annex sketched by the blue footprint adjacent to the left side of the main building. The target area E2 will be facilitated for VEGA system-related experiments in the future.

beamlines with nominal peak of powers P_{HPLS} = 100 TW, 1 PW, and 10 PW. All three beamlines have a dual-arm architecture and are fed by the central laser source. For achieving the high powers, an optical parametric chirped-pulse amplification (OPCPA) front end was implemented, which relies on state-of-the-art Ti:Sa crystals and dedicated pulse compressors. Coherent addition of the two strongest laser pulses from the two separated laser arms will result in powers larger than 20 PW. The layout of the whole experimental area at ELI-NP is depicted in Fig. 1.

Table I summarizes the core parameters associated with the driving laser source, which apply to all three different HPLS beamlines. In this table, λ_0 denotes the range of the central wavelength and $\delta\lambda_0$ its spread. τ_{LP} denotes the pulse duration, d_{full} the full diameter of the laser beam, S its Strehl ratio, and δa_{rel} the beam pointing stability.

Tests performed in early 2019 showed that the output energy for each of the three amplifiers in each arm can be expected to exceed the levels corresponding to the nominal powers P_{HPLS} after compression.[8] An in-depth publication of the measurement by Dancus *et al.* is forthcoming.[9] A Strehl ratio S = 0.95 was confirmed in a test experiment with P = 3 PW. The HPLS systems are serving a total of five dedicated target areas E1, E4, E5, E6, and E7, as depicted in Fig. 1. Table II lists the core operational parameters associated with the three different HPLS. In this table, I_0^{max} denotes the maximum achievable intensity after focusing with the appropriate mirror in a specific target station, E_{LP} denotes the range of energies for a single laser pulse for which safe operation is guaranteed by Thales, and f_{LP} denotes the pulse frequency. It is worth pointing out that the 10 PW system will allow one shot per minute.

The laser beam transport system (LBTS) is the interface between the HPLS and the five target areas E1, E4, E5, E6, and E7. As sketched in Fig. 1, it allows the transportation of the laser pulses to the large experimental chambers under vacuum in a specific target area. The LBTS has several subsystems, which include laser beam turn boxes and the vacuum system. The turn boxes host large-aperture mirrors, and the vacuum system includes pipes, gate valves with a diameter of 80 cm, and pumps to secure the high vacuum along the laser pulse propagation path. Some of these structures are very detailed and are omitted in Fig. 1 for clarity. Implementation of the LBTS is going according to schedule, and the testing of the installed system started in November 2019. The two 10 PW beams are routed to each interaction chamber using a minimum number of mirrors to reduce the complexity of the system and the maintenance costs.

The pulses of the 100 TW HPLS are transported to the experimental area E4, where an experimental campaign is already in preparation to study the laser-induced damage threshold (LIDT) for mirror coatings irradiated with $\tau_{LP} \lesssim 22.5$ fs and E_{LP} = 2.5 J. This will be the first experiment with the HPLS (March 2020). The 1 PW pulses are transported to the experimental areas E5 and, for commissioning experiments, to E7. The LBTS allows routing of the 10 PW pulses to the target areas E1 and E6, as well as also to E7 at a later stage of operation. For additional details related to the experimental target areas, including the scientific motivation and selected detector equipment, see Table III. In Fig. 1, the HPLS target areas E1, E6, and E7 are shown in white on the left of the figure. The first areas to be fully implemented, E4 and E5, which are served by the 100 TW and 1 PW arms of the HPLS, are displayed against a green background in the figure. The flat large-aperture mirrors and their corresponding motion systems allow high-resolution positioning of the beam at the entrance of an experimental chamber. Specific alignment and diagnostic devices provide the information that allows beam positioning within the LBTS. The LBTS control system enables routing of the beam and the operation of the vacuum. More details about the HPLS and LBTS have been reported in an earlier publication by Gales *et al.*[6]

The VEGA system is separate from the HPLS except for target area E7, where high-power laser pulses and high-intensity γ flashes up to 19.5 MeV with a very high linear polarization of >95% can be combined to allow nuclear experiments. The associated target areas E3, E8, and the newly installed E9 annex are also shown in Fig. 1.

B. The target areas at ELI-NP

The core parameters of the HPLS at ELI-NP, which are shared between all three beamlines present, are given in Table II, with the HPLS systems identified by their nominal power P_{HPLS}. Table III gives a full overview of the five target areas associated with the HPLS and includes a brief summary of the scientific motivation as well as a selection of the related detector systems. Laser core parameters such as the focal number of the focusing mirror f, the diameter relating to 90% of the focal spot intensity d_{90}^{f}, the associated Rayleigh length z_R, and the maximum value achievable for the dimensionless laser parameter a_0 are also provided. For E5, where the implementation of short- and long-focal-length mirrors is foreseen, both f_s and f_ℓ are shown in Table III.

With the parameters given in Table III, one can deduce the range of intensities I_0 achievable by an individual HPLS target area as presented in Fig. 2.

As mentioned before, target stations E3, E8, and E9 are solely dedicated to the VEGA system and are disjoint from the HPLS. Target station E7 is an exception, since the γ beam can be used for experiments in conjunction with the laser pulse from the 10 PW HPLS. Table IV gives a summary of the four target areas that are associated with the VEGA system at ELI-NP, briefly sketching the scientific motivation as well as highlighting a selection of detectors to be used in those areas. A more concise description of the selected detector systems will be given in Sec. IV (see Table VII). The associated maximum limit of E_γ is shown, as well as the expected full diameter of the γ beam, d_γ.

III. INAUGURAL EXPERIMENTS WITH THE HPLS AT ELI-NP

High-power laser systems are at the dawn of a new era in accelerator technology, and efforts are concentrated on exploiting new

TABLE I. Laser system parameters shared by the three HPLS beamlines at ELI-NP.

λ_0 (nm)	$\delta\lambda_0$ (nm)	τ_{LP} (fs)	d_{full} (mm)	S	Contrast	δa_{rel} (μrad)
814–825	55–65	15–22.5	550	0.80–0.95	$1:10^{13}$	$\lesssim 3$

TABLE II. Operational parameters of the three HPLS beamlines at ELI-NP.

P_{HPLS}	E_{LP} (J)	$\approx I_0^{max}$ (W cm^{-2})	f_{LP} (Hz)	Areas	Operational
10 PW	150–225	10^{23}	0.017	E1, E6, E7[a]	2021
1 PW	15–25	5.6×10^{21}	1	E1, E5, E6, E7[b]	2020
100 TW	1.5–2.5	2.2×10^{20}	10	E4	2020

[a]After commissioning experiments.
[b]During commissioning experiments.

acceleration regimes that efficiently transfer laser energy into particle and γ/X-ray beams at hitherto unmatched peak intensities I_0. As the maximum achievable I_0 is continually growing owing to technological advances, new routes for the scientific investigation of nuclear phenomena, particle and γ-ray source generation, and quantum electrodynamics (QED), as well as potential applications with societal impact, are being developed.[4,10–12] At ELI-NP, two experimental areas E1 and E6, are fully dedicated to this research, and both will be capable of utilizing two laser beams with a power of up to 10 PW each.[13] Before their installation is finished, initial tests relating to the research summarized above will be carried out at the 1 PW beamline at E5.

The commissioning experiments are aimed at investigating ion acceleration and QED effects via the generation of ultraintense particle and γ-beam flares.[6] The associated scaling laws governing

TABLE III. Summary of the three HPLS at ELI-NP, including associated target station areas, summaries of the physical motivations, and selected detector equipment, as well as specific laser parameters. The detector equipment listed will be explicitly described in Table V (active detectors) and VI (passive detectors) in Sec. III.

HPLS: 10 PW and 1 PW for commissioning studies			
Area	Motivation	Detectors	Parameters
E1	Nuclear physics experiments with *solid* targets, production of high fluxes of energetic ion beams (ideally monoenergetic) and neutrons, and intense X-ray flares	Thomson parabola, gamma spectrometer, e^-–e^+ spectrometer, CsI(Tl) spectrometer, activation foils, image plates, radiochromic films, CR-39 resin, and optical plasma probe	f/2.7 $d_{90}^{f} \gtrsim 3.5\,\mu$m $z_R \approx 15\,\mu$m $a_0 \lesssim 220$
E6	QED and nuclear physics experiments with *gas* targets, production of GeV electrons at high intensity for radiation reaction studies	GeV e^- spectrometer and optical plasma probe	f/54 $d_{90}^{f} \gtrsim 60\,\mu$m $z_R \approx 4$ mm $a_0 \lesssim 16$
HPLS: 1 PW			
Area	Motivation	Detectors	Parameters
E5	Applied experiments, medical research, production of MeV ions, and preliminary studies for 10 PW system using *gas* and *solid* targets	As for E1, but modified for E5 setup where necessary	f_s/3.5 and f_ℓ/24[a] $d_{90,s}^{f} \gtrsim 5\,\mu$m $z_{R,s} \approx 25\,\mu$m $a_{0,s} \lesssim 50$
E7[b]	Combined laser and γ radiation experiments, production and photoexcitation of isomers, radiation reaction, pair production in the extremely nonlinear regime, vacuum birefringence	Gamma-Polari-Calorimeter	f/15 $d_{90}^{f} \gtrsim 18\,\mu$m $z_R \approx 450\,\mu$m $a_0 \lesssim 12$
HPLS: 100 TW			
Area	Motivation	Detectors	Parameters
E4	Fundamental physics, QED-based elastic γ–γ scattering, search for weakly coupling sub-eV dark matter	Instrumentation to be developed	f/6 $d_{90}^{f} \gtrsim 8\,\mu$m $z_R \approx 70\,\mu$m $a_0 \lesssim 10$

[a]For long parabola f_ℓ/24: $d_{90,\ell}^{f} \gtrsim 24\,\mu$m, $z_{R,\ell} \approx 230\,\mu$m and $a_{0,\ell} \lesssim 10$.
[b]Upgrade to the 10 PW HPLS arms after commissioning experiments.

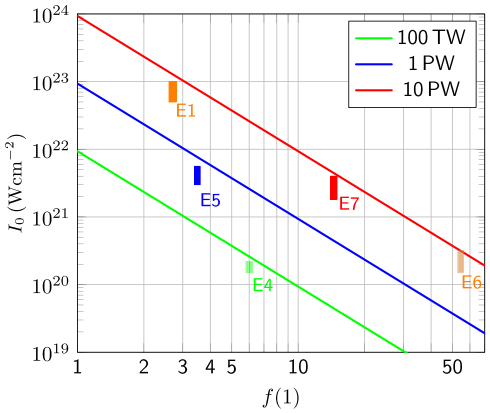

FIG. 2. Nominal peak intensity ranges I_0 as functions of the f number of the focusing mirrors installed at the target areas E1, E4, E5, E6, and E7 associated with the HPLS beams at ELI-NP. The solid lines describe the ideal case at the diffraction limit for which I_0 is at its maximum value.

these regimes will be deduced in analogy to the work presented by, for example, Fuchs *et al.*[14] Moreover, the theoretical predictions obtained using particle-in-cell (PIC)-based codes[15] can be evaluated. Achieving maximum kinetic proton energies $E_p^{\max}$ around and above 200 MeV with minimized energy spread δE_p is one of the core aims envisaged in the commissioning campaign. This research will naturally progress by studying different acceleration regimes to optimize secondary ion sources for various applications, with particular emphasis on nuclear physics.[16] If the predicted results are attained, a new era in acceleration technology will begin, as envisaged in the original paper by Veksler[17] more than 60 years ago. Additionally, to spearhead the development of ultraintense laser-driven γ-ray sources, the optimization of the laser (energy)-to-γ-radiation conversion based on the onset of QED effects is of paramount interest in the inaugural campaign. Furthermore, the production of intense ultrarelativistic electron and positron beams and of coherent betatron radiation will be extensively studied.

A. Theoretical considerations

1. Ion acceleration

The complexity of the laser–matter interaction encompasses a manifold of ion acceleration regimes distinguishable by a set of parameters. For the HPLS, these are its intensity I_0, the related pulse duration τ_{LP}, and its temporal profile. The most crucial parameters relating to the target are its electron density n_e and its thickness ℓ_{T}. In the last two decades, several acceleration regimes have been experimentally identified. Additionally, the existence of further, very exotic regimes is predicted based on PIC simulations. The laser intensity I_0 is often represented using the dimensionless laser amplitude a_0. Its value for linear polarization is given by

$$a_0 = \frac{eE_0}{m_e c\omega} = \sqrt{\frac{I_0\lambda_0^2}{1.37\times 10^{18}\ \mathrm{Wcm^{-2}}\,(\mu\mathrm{m}/\lambda)^2}}, \tag{1}$$

with e and m_e the electron charge and mass, and c the speed of light in vacuum. Furthermore, E_0, λ_0, and ω denote the maximum electric field amplitude, wavelength, and angular frequency of the laser, respectively.[18] Depending on the acceleration mechanism, the target thickness ℓ_{T} or the dimensionless areal density $\sigma = n_e\ell_{\mathrm{T}}/n_{\mathrm{cr}}\lambda$ is used to describe the scaling laws. Figure 3 illustrates the acceleration regimes based on current measurements and simulations. The most prominent regimes that can be studied at ELI-NP are the target normal sheath acceleration (TNSA),[19] the Coulomb explosion (CE),[20] and the

TABLE IV. Summary of the target areas associated with the VEGA system, motivation, selected detector equipment, and specific parameters. The detector equipment shown will be explicitly described in Table VII in Sec. IV. The use of area E2 is yet to be decided.

Areas	Motivation	Detectors	Parameters
E3	Slow positron beamline for material science and characterization, structural and defect studies of metals, semi-conductors and insulators	Positron annihilation lifetime spectroscopy system (PALS), positron annihilation-induced Auger electron spectroscopy system (PAES)	$E_\gamma \le 3.5$ MeV $d_\gamma \approx 6$ mm
E7	γ-induced charged particle reactions for astrophysics and photofission experiments	Electronic time-projection chamber (ELITPC), array of twin Bragg ionization fission chambers (ELI-BIC), thick gas electron multiplier detectors (ELITHGEM)	$E_\gamma \le 19.5$ MeV $d_\gamma \approx 0.75$ mm
E8	γ-induced charged particle reactions for astrophysics and photofission experiments, NRF experiments with high-energy γ rays for basic and applied research	Segmented silicon detector array (ELISSA), array of segmented high-purity germanium clover detectors (ELIADE)	$E_\gamma \le 19.5$ MeV $d_\gamma \approx 1.25$ mm
E9	γ-induced reactions above the neutron threshold for basic and applied research	Moderated array of ^{3}He tubes (ELIGANT-TN), array of liquid scintillators and lithium glass scintillators, large-volume $LaBr_3$(Ce) and $CeBr_3$ scintillators (ELIGANT-GN)	$E_\gamma \le 19.5$ MeV $d_\gamma \approx 2.5$ mm

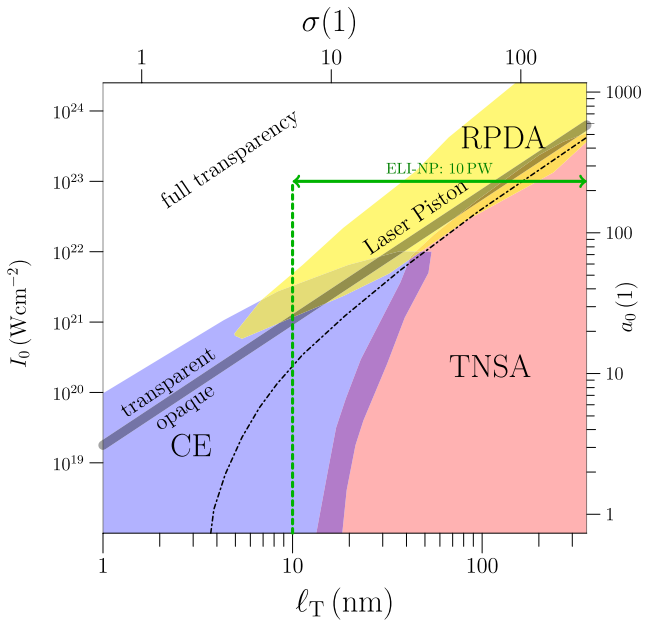

FIG. 3. Regimes of laser-driven ion acceleration with Coulomb explosion (CE), target normal sheath acceleration (TNSA), and radiation-pressure-dominated acceleration (RPDA). The gray line indicates the opaque/transparent border and the dashed line the target thickness ℓ_T for which the proton energy at a given I_0 will be maximal. The regimes overlap in certain parameter regions. Intensity conditions, as indicated by the green arrow, should be reachable with the ELI-NP 10 PW HPLS, employing self-supporting targets as thin as 10 nm. The regimes as depicted in this figure follow published work by Daido *et al.*[18]

radiation-pressure-dominated acceleration (RPDA).[16,21] As of today, TNSA is the most extensively studied regime. Within this regime, the laser light is interacting with the front side of the target and generates relativistic electrons that can cross the target bulk, setting up a plasma sheath, which generates a strong electric field between the electron cloud and the target surface. For extremely high laser intensity, under suitable conditions of laser–matter interaction, RPDA can dominate the acceleration process by means of the so-called hole boring (HB) or light sail (LS) mechanisms for thin target foils. In that case, the electrons are pushed forward during the first laser cycle owing to the radiation pressure, and the ions respond promptly to this charge displacement and the associated strong **E** field. This generates synchronous motion between electrons and ions, making the target bulk "fly" and accelerate continuously during the laser push, even reaching relativistic velocities ("relativistic flying mirror"). In this instance, most of the laser energy is efficiently transferred to the target ions. The maximum kinetic energy per nucleon with n nucleons, E^m/n, for such an ideal laser–target coupling can be expressed as

$$E^m/n = m_p c^2 \frac{2F^2}{2c^2F\sigma + c^4\sigma^2}, \quad (2)$$

where m_pc^2 is the proton mass–energy equivalent of 931.5 MeV, with c being the speed of light, σ is the areal density of the target, and F is the total laser fluence, i.e., the laser pulse energy E_{LP} divided by the laser focal spot area.[11]

For targets of limited length, typically smaller than the laser wavelength λ_0, CE will take place. If the laser is intense enough to expel all electrons from the region of interaction, then only a bare ion core is left. The electrostatic field created by the space charge then leads to a CE. This field is the most intense that can be generated under any electron–ion charge displacement conditions. This process can be best realized by employing small clusters such as those created by a low-temperature gas jet. It is important to note that the borders among these regimes are not sharp, and hybrids exist. Moreover, for ultrathin foils (e.g., of the order of tens of nanometers), the onset of relativistic induced transparency (RIT) has to be considered if $I_0 \gtrsim 10^{21}$ W cm^{-2} where RIT occurs owing to the relativistic increase in the inertia of the electrons ($m_e' = \gamma m_e$), which decreases the plasma frequency ω_p, thus increasing the plasma critical density.[22–24] The lower density acts like an aperture in the target, and strong electric and magnetic field amplitudes of the order of $E_0 \sim 50$ TV m^{-1} and $B_0 \sim 0.5$ MT enable laser pulse propagation throughout the plasma. This, in turn, enhances E_p^{max} and, at the same time, reduces the energy spread of the beam.[25] As a tradeoff related to RIT, the overall conversion efficiency ε_{conv} is limited, since the momentum transfer from the pulse to the foil is optimal for opaque conditions. Recently, enhancement of E_p^{max} due to RIT has been experimentally shown by Higginson *et al.*,[26] who achieved $E_p^{max} \approx 100$ MeV within a hybrid TNSA–RIT scheme. This value is currently the record for laser-accelerated ions.

To estimate the proton energy at ELI-NP achievable in the commissioning experiments with the 10 PW systems that can provide an intensity $I_0 \sim 10^{23}$ W cm^{-2} (i.e., $a_0 \sim 220$), PIC2D simulations were performed (using the Epoch code[27]) for a solid target with $\ell_T = 800$ nm. The results are depicted in Fig. 4, which shows the proton and γ-ray spectra as well as the spectrum for fully ionized carbon ions for a CH_2 target with $\ell_T = 800$ nm irradiated at $I_0 = 10^{23}$ W cm^{-2}.

If correct, the commissioning experiments should lead to a maximum proton energy $E_p^{max} \approx 400$ MeV exhibiting the typical Maxwell–Boltzmann distribution as shown in Fig. 4. The total efficiency of laser-to-γ conversion in the region is estimated to be around 14%. In these calculations, no preplasma modeling was included. A

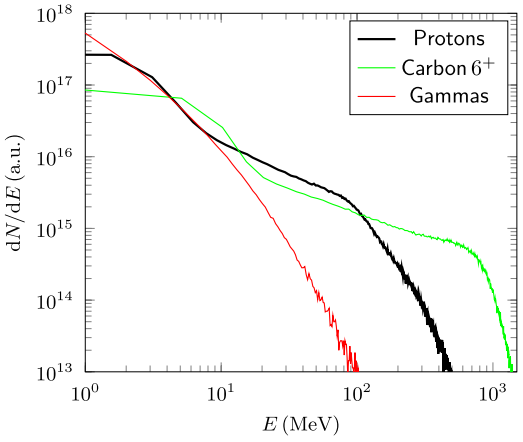

FIG. 4. Energy spectra of protons (black), C^{6+} (green), and γ radiation (red) emitted in the direction of pulse propagation according to a PIC2D-based Epoch code[28] including QED effects. A circularly polarized laser beam of intensity 10^{23} W cm^{-2} and a fully ionized CH_2 target with $\ell_T = 800$ nm were assumed.

substantial amount of the related high-energy γ radiation will be emitted in a backward direction with respect to the incident laser beam propagation axis.

Investigations in the CE regime facilitating the gas target station at E6 are predicted to result in similar energies. Esirperkov *et al.* give a scaling law

$$\frac{E_{\rm ion}}{Z_{\rm ion}} \sim 230\ {\rm MeV}\sqrt{P_{\rm LP}/{\rm PW}}, \tag{3}$$

with $Z_{\rm ion}$ being the charge of the accelerated ion and $P_{\rm LP}$/PW the power of the laser pulse in units of petawatts.[16,18] Figure 3 illustrates various ion acceleration regimes as a function of the target thickness (horizontal axis) and the laser intensity (vertical axis).

2. Ultrarelativistic electron acceleration

The generation of ultrarelativistic electrons via laser wakefield acceleration (LWFA) is an important new field of plasma physics, both as a tool for testing QED theory and for applications involving leptons and γ rays. Since the original idea of Tajima and Dawson,[29] a lot of research has been dedicated to studying different electron acceleration mechanisms.[30] Nowadays, most LWFA experiments are based on wave-breaking, or self-injection, where the electrons are injected into the wave. There are also some other injection schemes that do not rely on self-injection.[31] Using the so-called "bubble" regime, it has been shown that quasi-monoenergetic electron beams can be produced in bunches of tens of femtoseconds. The accelerating field generated in the wake is of the order of 100 GeV m^{-1}, and the electrons can be accelerated for many centimeters, if the prevailing interaction conditions are ideal. The experimental area E6 will be dedicated to generic electron acceleration studies first, followed by QED experiments. The two laser arms of the HPLS are focused by a long-focal-length (32 m) spherical mirror with ~f/54 and a short-focal-length (2 m) parabolic mirror with ~f/3.5. The long-focal-length mirror will be used to generate the electron beam, while the short-focal-length mirror will be used to shoot a counterpropagating second laser pulse against the electrons beam, providing the conditions for entry into the strong-field QED regime.[32] The commissioning experiments at E6 will be dedicated to the generation of stable multi-GeV electron beams with high charge exhibiting a quasi-monoenergetic distribution. As shown in Table III, each 10 PW laser arm has an energy of ~225 J and a pulse duration $\tau_{\rm LP} \lesssim 22.5$ fs. However, with a focusing mirror of ~f/54, the optimum LWFA conditions require a longer pulse (namely, ~100 fs). Therefore, there is a need to stretch the laser pulse. An optimal acceleration can produce electron beams of energy in excess of 5 GeV, over an acceleration distance greater than 10 cm.[33] The beams will be diagnosed by a permanent magnetic spectrometer for electron and positron detection. The gas cell will be probed optically by interferometry and shadowgraphy with an ultrashort laser beam, and the electron bunch charge and the betatron emission will be measured as well. Further, after the interaction, the laser pulse will have residual energy, which will give a flux of the order of 10^{15} W cm^{-2} at a distance 10 cm away from the gas target. This value exceeds the damage threshold of any material. Hence, a metallic foil will be employed as the laser beam dump. An electron beam dump for electron energies $E_e > 5$ GeV will also be utilized in the region near the GeV e^- spectrometer.

3. Laser-to-γ conversion

According to theory, the distribution of the initial laser energy $E_{\rm LP}$ between ion acceleration, e^- acceleration, and γ radiation/X-rays changes dramatically with increasing laser intensity represented by a growing a_0. It is calculated that laser-to-γ conversion will be dramatically enhanced. This is due to the onset of nonlinear Thomson scattering in the QED regime wherein the energy of the photons E_γ is given by $E_\gamma = 0.3\hbar\omega a_0^3$. For $a_0 \approx 220$, the maximum photon energy E_γ is in the hundreds of MeV energy range.[34] Hence, strong coupling between the laser pulse and the solid matter in which the pulse propagates can be assumed. Moreover, the onset of radiation friction leads to self-focusing patterns via magnetic fields. This, in turn, limits the transverse phase space of the electrons and traps them efficiently in the laser-produced channel, where they undergo betatron oscillation imposed by the quasistatic electromagnetic fields.[35] The radiation is partially coherent, showing a significant broadening of the resonance condition and an exponential shape. For an initial laser power raising from 1 PW to 10 PW, the conversion efficiency from laser to γ rays can increase rapidly from a few percent to $\varepsilon_\gamma \sim 30\%$ for a target made of light ions, as predicted by PIC simulations.[36] For such conditions, the 10 PW system can be seen as an ideal transformer from light into γ radiation. The calculations also show that the high-energy photon part of the photon beam can reach more than 100 MeV, being aligned either parallel or antiparallel to the propagation direction of the laser. Besides a_0, the atomic mass $m_{\rm i}$ of the production target is a crucial parameter in the related theoretical evaluations for $I_0 > 10^{22}$ W cm^{-2}. For $E_\gamma < 20$ MeV, the radiation pattern becomes more and more isotropic. γ flares are predicted to have a maximum yield in the backward direction if heavy-ion production targets are used.[37] For optimization of the γ yield, preplasma engineering is required.

The use of a tailored overcritical-density target for which the laser pulse to γ-ray energy conversion efficiency is substantial is mandatory. With $I_0 \approx 10^{23}$ W cm^{-2}, a peak brightness of $n_\gamma \gtrsim 10^{25}$ ps^{-1} mm^{-2} mrad^{-2} (1% BW)$^{-1}$ at 15 MeV should be achievable with the ELI-NP 10 PW arms in the commissioning experiments.

B. Experimental considerations and diagnostics

The design strategy for the HPLS at ELI-NP followed the necessity to separate solid and gas target stations as debris mitigation, and nuclear shielding requirements differ substantially depending on the nature of the target and the produced radioactive radiation (see Table III). Hence, the E1 target chamber at ELI-NP is dedicated solely to the study of laser-plasma interaction with solid targets, while the E6 chamber, similar in dimensions, is exclusively for gas targets. At E1, one has to consider the measurement of fast ions, electrons, and neutrons, as well as high-intensity γ flares, while equipment at E6 has mainly to be aligned to handle relativistic electrons and the highest photon fluxes. Furthermore, to protect the off-axis parabolic mirror and the HPLS, a sacrificial plasma mirror system is expected to be installed in E1 just a few centimeters away from the front of the primary production target. For long-term development, the introduction of circular polarization (CP) is suggested, since it helps to reduce $\mathbf{J} \times \mathbf{B}$ electron heating, which otherwise would lead to more rapid deterioration of the target and de-optimize the acceleration process. Both target stations are connected to the two 10 PW HPLS

arms and can also source the two 1 PW HPLS arms used for inaugural studies.

Since ELI-NP, like all other HPLS, operates in a high-intensity, low-repetition-rate mode, one has to implement a new strategy for the diagnostics to record the manifold nuclear phenomena induced by short-pulsed intensive particle and radiation beams. Moreover, to understand the different acceleration and conversion processes, laser and plasma characterization will also be performed *in situ* with optical probing techniques on a shot-to-shot basis. A particular challenge is given by the fact that the time scales for beam production are in the femtosecond regime and much shorter than the typical pulse shaping and acquisition times of any electronically based detection system.

For all the related development, special attention has to be given to the expected strong background caused mainly by bremsstrahlung. The associated noise will lead to a gamut of soft and hard X rays, which will make the greatest contribution to the unwanted background signal on pulse impact. Direct reactions from the produced ions and neutrons may also introduce a coinciding nuclear radiation background. To account for those instances, in line with radioprotection considerations and detector and shielding design optimizations, Fluka[38] simulations were undertaken to evaluate the radiation levels expected at the E1 and E6 target chambers and to optimize the signal-to-noise ratio (S/N) for each detector. Another noise-enhancing factor is the unavoidable induction of an electromagnetic pulse (EMP) generated by the laser–matter interaction.[39] An ELI-NP study by Meade[40] concluded that, to first order, the EMP-induced background scales linearly with the energy E_{LP} of the laser pulse and is proportional, to a lesser extent, to I_0. Owing to the high background level and the diverse background sources, the detector systems are foreseen to facilitate optical readouts via fiberglass cables, which feed into high-resolution cameras placed outside the interaction chamber. As for the ion generation studies, a 10^{13} suppression of the prepulse is guaranteed by Thales. To minimize the intruding effects of the prepulse formation even further, a thin plasma mirror system using a film with a thickness of $\ell \approx 10$ nm will be tested.

1. Diagnostics development and nuclear detector systems

Since no laser-plasma interactions with a 10 PW system and intensities of $I_0 \sim 10^{23}$ W cm^{-2} have ever been measured, the design of robust nuclear diagnostic tools has to be based solely on simulations and the extrapolation of existing measurements, for which intensities are about one full order of magnitude smaller. Over a decade ago, Chen *et al.*[41] summarized suitable detection systems for laser-plasma experiments with $I_0 \lesssim 10^{20}$ W cm^{-2}, providing a benchmark to follow for the ELI-NP implementation. For the commissioning experiments, the energy ranges and the corresponding energy resolution for the currently existing standard particle and photon detector systems need to be extended. This translates into, for example, estimating a value for S/N and guaranteeing fail-safe operation of the detectors, as well as protecting the HPLS. Besides that, a characterization of the laser pulse at a full-power shot, before and after the interaction with the target, will be done, as well as measurement of the plasma density using interferometry. In the following paragraphs, a selection of core detection and diagnostic devices to be used in E1, E5, and E6 are presented. It is worth noting that their design is still being optimized, and their exact positioning in the target station will have to be decided on an experiment-to-experiment basis. A precalibration of specific detectors will be undertaken at an RF-based accelerator system, such as a linear accelerator (LINAC) before the commissioning laser experiments take place. At this very moment, all instrumentation introduced is being developed, and Technical Design Reports (TDRs) are currently being finalized, with purchase tenders released. The construction of the instrumentation and the calibration measurements are on target for completion on schedule. Most of the performance parameters presented are based on simulation programs, such as Geant4, Simion, and Fluka.[38,42,43] A summary of *active*, *passive*, and *optical* detection systems depicted in this section is given in Table V for the active and Table VI for the passive detectors.

a. Thomson parabola (ion spectrometer). Measurements performed on the Thomson parabola give information about the ion species produced by a laser pulse and the associated energy distributions.[44–46] The Thomson parabola for E1 will have a large dynamic range catering for proton energies of up to $E_p \approx 250$ MeV, with a small relative uncertainty of $\delta E_p/E_p < 0.65\%$ as derived from simulations. The pinhole at the front of the Thomson parabola will be 0.2 mm in diameter. If placed 1.5 m away from the interaction target, the Thomson parabola will cover a solid angle of $\Omega_{geo} = 1.5 \times 10^{-8}$ sr. The core of the parabola consists of one permanent magnetic dipole with $|\mathbf{B}| = 1.0$ T and an electrostatic deflector at a potential of 26 kV. For measurement of the deflected ions, a LANEX detection screen will be installed. In contrast to, for example, a multichannel plate (MCP) detector, the LANEX screen also permits fail-safe operation for non-ideal vacuum pressure levels to be expected during the commissioning campaign with $p \gtrsim 10^{-5}$ mbar. An all-optical readout of the signals will feed online into a CCD camera, allowing data acquisition in the Hz regime and flexible positioning of the detector system within the E1 target chamber. The actual design of the Thomson parabola was based on simulations with the program[43] in which proton energies in the range of 20–250 MeV were assumed. For carbon ions, the energy range covered was 1–160 MeV A^{-1}. The low angular acceptance allows minimization of the EMP and γ/X-ray-induced background. The entrance of the Thomson parabola in E1 will also be enclosed by an 8 cm thick lead case to suppress the background noise and thus improve the S/N level. For details, see Fig. 7(b). Another Thomson parabola is planned to be implemented at E5, which will cater for proton energies of up to $E_p = 100$ MeV.

b. The forward Compton gamma spectrometer. The characterization of the energy and angular distribution of the γ/X rays is a significant factor in understanding the complex aspects of the laser–target interaction at a 10 PW system. As the intensities are so high and the times associated with the processes are so short (typically 30–80 fs), conventional detection methods employed in traditional γ-spectroscopy measurements, such as high-purity germanium (HPGe) detectors, are not suitable. The flashes are predicted to have a maximum energy of around 100 MeV, with their yield distribution peaking somewhere between $E_\gamma \sim 5$ MeV and $E_\gamma \sim 12$ MeV. The radiation burst exhibits an almost spherical symmetry for lower energies while showing distinct peaks in either in the forward or

TABLE V. Summary of *active* detectors in the target areas E1, E5, and E6 to be used in inaugural commissioning experiments facilitating the HPLS.

Detector and purpose	Areas	Parameters
Thomson parabola: For energy spectra of ions	E1, E5	OP: Ion deflection in static field $\|\mathbf{E}\| = 26$ kV cm^{-1} and $\|\mathbf{B}\| = 1.0$ T; $E_p \lesssim 250$ MeV (E5: $\lesssim 100$ MeV); $\delta E_p \lesssim 1.6$ MeV (E5: $\lesssim 0.8$ MeV); S/N $\gtrsim 3$ db; $\Omega_{geo}(1.5\ \text{m}) = 1.5 \times 10^{-8}$ sr. Dimensions: 10 cm × 20 cm × 100 cm. Weight: 220 kg. Shielding: Encased Pb: 8 cm at front; 3 cm at sides, back and top. No.: ≤3. Readout: Optical, LANEX screen.
Gamma spectrometer: For γ-radiation up to $E_\gamma = 50$ MeV	E1, E5	OP: Conversion of γ radiation with Li target, measurement of diametrically deflected e^-–e^+ pairs with opposing LANEX screens, deflection via a magnetic field with $\|\mathbf{B}\| = 0.5$ T; $E_\gamma = 5$–50 MeV; $\delta E_\gamma \leq 20\%$; S/N $\gtrsim 10$ db, $\epsilon_{tot} = 10^{-8}$–5×10^{-8}. Dimensions: 35 cm × 35 cm × 60 cm. Weight: 380 kg. Shielding: Encased Pb: 30 cm at front, 2 cm Fe at sides, back and bottom. No.: 1. Readout: Optical, LANEX screen.
e^-–e^+ spectrometer: For e^- up to $E_{e^-} = 100$ MeV	E1, E5	OP: Measurement of e^- and e^+ after deflection by magnetic field ($\|\mathbf{B}\| = 0.8$ T) with LANEX screens, identical build to gamma spectrometer (but without Li converter); $E_\gamma = 5$–100 MeV; $\delta E_\gamma \leq 5\%$; S/N $\gtrsim 10$ db. Dimensions, Weight, Shielding, No., Readout: Identical to gamma spectrometer.
CsI(Tl) gamma spectrometer: For γ-radiation up to $E_\gamma = 20$ MeV	E1, E5	OP: Measurement of segmented scintillation units, 10 layers of 5 mm thick CsI(Tl) scintillation layers, energy spectrum of γ radiation estimated after deconvolution of measured spectra; $E_\gamma = 2$–20 MeV; $\delta E_\gamma \sim$ 30%–40%. Dimensions: 20 cm × 15 cm × 15 cm. Weight: 20 kg; Shielding: Encased Pb-canvas ~1.5 cm. No.: 5. Readout: Optical from scintillator units.
GeV e^- spectrometer: For e^- up to $E_{e^-} = 5$ GeV	E6	OP: Measurement of e^- deflection by magnetic field of $\|\mathbf{B}\| = 1$ T with LANEX screen; $E_\gamma = 100$ MeV–5 GeV; $\delta E_\gamma \lesssim 10\%$; $\Delta\Theta = \pm 10$ mrad. Dimensions: 36 cm × 25 cm × 80 cm (dipole). Weight:680 kg. No.: 1. Readout: Optical, LANEX screen.

backward direction for high-energy radiation ($E_\gamma > 10$ MeV). The exact radial distributions are complex and depend, among other things, on the atomic mass number A of the production target.[36,47]

The detector design for the forward Compton gamma spectrometer is aimed to overcome current limitations imposed by existing technologies in the field of single-shot γ/X-ray spectroscopy. Schematics of the side and front cross-sectional views of the spectrometer are shown in Fig. 5. The design follows, in essence, the successful demonstration of a similar prototype, the Global Spectrometer for Positron and Electron Characterization (GSPEC) at the Texas Petawatt Laser by Glenn *et al.*[48]

Core to the improvement is the use of a permanent magnet with $|\mathbf{B}| = 0.5$ T to deflect the emerging electron–positron (e^-–e^+) pairs, which produce a background signal, in opposite directions as depicted in Figs. 6 and 7(a). As such, this two-plate configuration differs substantially from detector concepts presented, for example, by Singh *et al.*,[49] where only one image plate is used. The measurement will permit subtraction of the pair production background in the offline analysis and hence, according to Geant4 simulations, allow the detection of γ energies in the range of 5–50 MeV. Within that energy range, the relative energy resolution $\delta E_\gamma/E_\gamma$ will vary between 20% for $E_\gamma \lesssim 10$ MeV and 5% for $\delta E_\gamma/E_\gamma (\sim 50$ MeV) using a suitable reconstruction mechanism following the example of Haden *et al.*[50] The operational principle of the instrument relies on the forward-scattered Compton electrons emitted after the interaction of the incoming high-energy photons within a low-Z lithium converter target. These zero-degree scattered electrons carry the maximum possible energy from the process, which is close to the energy of the incident photon. The photon spectrum can be reconstructed with Monte Carlo simulations that take into account the energy difference between the incoming photon and the detected zero-degree electron, and the energy loss from the latter within the converter target. The method implies that the forward-scattered Compton electrons will give a strong signal on the detection screen that is above the noise level created by the electrons and positrons emitted in the parasitic pair creation process. Since the Compton scattering scales with the Z value of the material, but the pair creation process is proportional to Z^2, metallic lithium with $Z = 3$ is the ideal converter material to minimize the background signal. Simulations show that an S/N $\gtrsim 10$ db can be achieved. The permanent magnet with $|\mathbf{B}| = 0.5$ T will deflect the emerging electron–positron pairs, which produce a background signal, as depicted in Fig. 7(a), into opposite directions so that they impinge on the diametrically opposed image plates. Figure 6 shows the simulated distributions of the electron and positron pairs forming the background signal in the two opposing LANEX screens on which the S/N estimation as well as the other parameters depicted in Table V were based. It is important to point out that the background subtraction is undertaken in offline mode, since, owing to the rapidity of the signal in the sub-picosecond regime, no electronic coincidence system can be used.

TABLE VI. Summary of the *passive* and *optical* detector systems in the target areas E1, E5, and E6 to be used in inaugural commissioning experiments facilitating the HPLS.

Detector and purpose	Areas	Parameters
Activation: For k_BT for γ and E^{max} for ions	E1, E5	OP: Measurement of γ- or proton-induced nuclear reactions such as (γ, xn) or (p, n) exit channels. Isotopes for γ-induced reactions are ^{181}Ta, resulting in (γ, n) and $(\gamma, 3n)$ channels with $t_{1/2}(^{180}\text{Ta})$ = 8.15 h and $t_{1/2}(^{178}\text{Ta})$ = 2.36 h, as well as ^{12}C and ^{63}Cu, resulting in (γ, n) channels with $t_{1/2}(^{11}\text{C})$ = 20.36 min and $t_{1/2}(^{62}\text{Cu})$ = 9.67 min. For proton energy, e.g., the reaction $^{63}\text{Cu}(p,n)^{63}\text{Zn}$ with $t_{1/2}(^{63}\text{Zn})$ = 38.47 min will be used; typical $\Omega_{int} \lesssim 1$ sr. Weight: 1 kg. No.: 5–10. Readout: Offline with HPGe or NaI
RCF, image plates, and CR-39: For γ and ion energy spectra and radial distribution	E1, E5	OP: Measurement of γ- and ion-induced darkening of RCF or image plate fluorescence or traces within CR-39; E_γ is adjustable with attenuator stacks; typical $\Omega_{int} \lesssim 1$ sr. Weight: 1 kg. No.: 5–10. Readout: Optical with high-resolution scanning system
Optical plasma probe: For probing n_{e^-}	E1, E5, and E6	OP: Probing plasma electron density n_{e^-} with fundamental λ_0 and second-harmonic wavelength at ~410 nm. No.: 1. Readout: Optical (interferometry, shadowgraphy)

A thick encapsulated Pb shielding, which can be extended to 30 cm of thickness, will face the primary target position. According to Geant4 simulations with γ source energies up to 100 MeV, this will minimize the radiation background to acceptable levels. Assumed thicknesses larger than that did not show any significant improvement of S/N and would have become technically unfeasible owing to weight considerations. Ironclads with a thickness of 2 cm are deemed to provide sufficient background protection for the side walls. The spectrometer will be positioned inside the E1 interaction chamber, and can be installed at various angles of inclination at a minimum distance of 50 cm. Collimators with diameters of 10 mm, 15 mm, and 30 mm can be used, leading to a geometrical acceptance Ω_{geo} between 2.5×10^{-5} and 2.3×10^{-4}. The collimator length can be up to 30 cm and reduces the noise level induced by the scattered photons to a minimum. This makes a two-collimator setup as used in the recent work of Singh *et al.*[49] obsolete. Folding Ω_{geo} with the intrinsic detection efficiency deduced from simulations, a total efficiency ε_{tot} in the range of 1×10^{-8} to 5×10^{-8} at a detector distance of 50 cm is expected. Figure 7(a) depicts a model of the gamma spectrometer as used in Geant4 simulations. The γ rays are shown in green and are emitted from the laser target. They were interacting with the front shielding (gray) of the spectrometer and with the small Li converter target at the front (solid blue). Secondary produced electrons (thin red lines) and positrons (thin blue lines) are displayed as well. The two opposing LANEX screens (1 and 2) for electron and positron identification are horizontally aligned and depicted as light gray rectangles just below and above the parallel aligned separating magnets.

c. Prompt electron–positron spectrometer. The prompt electron–positron spectrometer is designed to allow an estimate of the produced electrons and positrons to evaluate the E_{LP} partition function. It is identical in design to the gamma spectrometer with regard to its overall mechanical structure and shielding arrangements, but differs in that no Li converter target is needed, and the permanent magnet used will have a

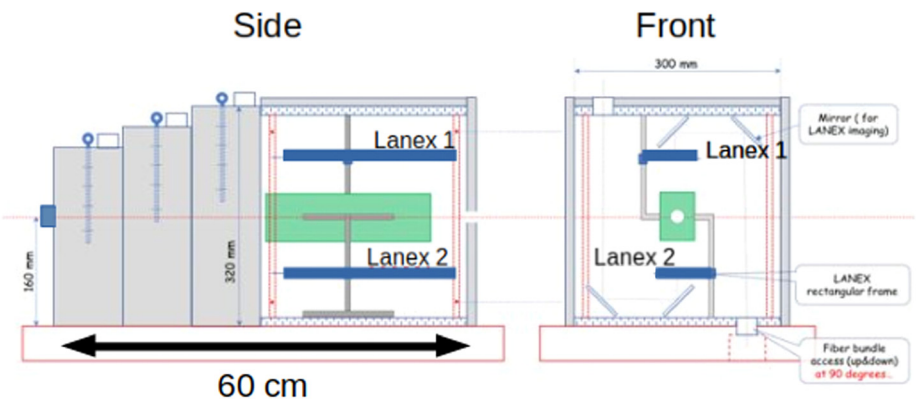

FIG. 5. Schematic side and front cross-sectional views of the gamma spectrometer. The two LANEX screens (1 and 2) are not to scale and are emphasized in dark blue, with their thicknesses enhanced. The Li converter at the entrance is shown in blue and the magnet with $|\mathbf{B}| = 0.5$ T is shown in green.

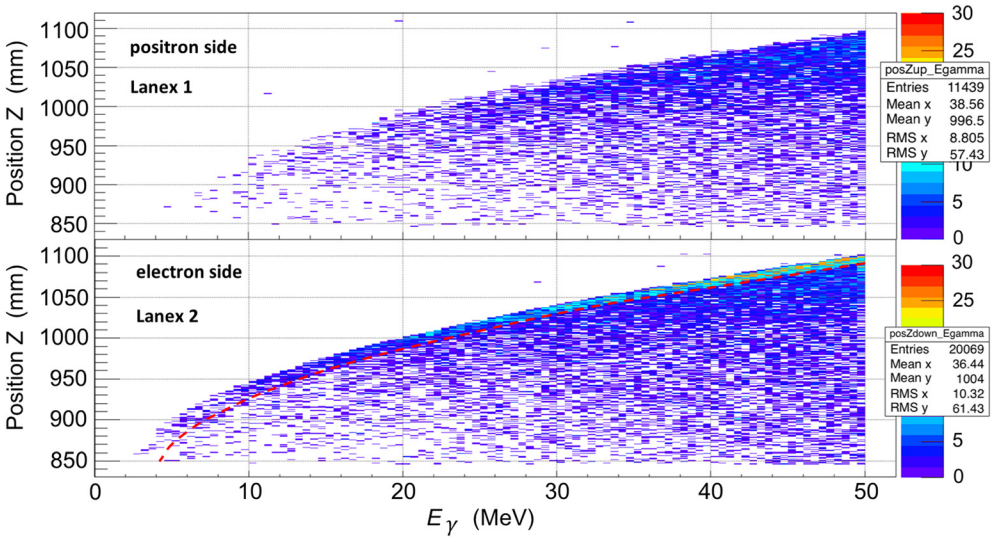

FIG. 6. Geant4 simulation of the strength of the background signal caused by the electron–positron pairs as expected in the two opposing LANEX screens, LANEX 1 (e^+, upper part) and LANEX 2 (e^-, lower part). A fictitious constant distribution of γ/X rays from 0 MeV to 50 MeV was assumed to estimate the S/N value. The Compton-scattered electrons are retrieved after the background electrons arising from pair production are subtracted from the total electron signal in LANEX 2. For this, the positron spectra in LANEX 1 are used. The red dashed line in the subplot for LANEX 2 represents the separation between the true signal due to the Compton-scattered electrons and the background signal as deduced from LANEX 1 in offline analysis.

stronger field $|\mathbf{B}| = 0.8$ T. The detector will allow measurement of kinetic energies up to $E_e \sim 100$ MeV, as expected from theoretical work.[47]

d. CsI(Tl) gamma spectrometer. An additional detector concept foresees the stacking of 10 CsI(Tl) scintillator plates (50 mm × 50 mm × 5 mm) interlaced with metallic attenuator sheets to characterize the γ/X-ray flares of up to ~20 MeV, following the works of, for example, Rhee *et al.*[51] and Rusby *et al.*[52] The detector design was based on Monte Carlo simulations using the Geant4 program.[53] Triggered by the incoming γ/X rays, light photons are emitted within the 5 mm thick scintillator plates. The light intensity is proportional to the energy loss of the radiation in the specific plate segment. The scintillation light is then transported via an optical fiber bunch to the outside of the interaction chamber and read by a high-resolution CCD camera before being processed by the reconstruction software, which uses a minimization procedure to reconstruct the original X-ray energy spectrum. Mathematically, this operation can be written as

$$\min_{e}\left[\sum_{i,e_b}\left(A_{e_b}M_{i,e_b}(\bar{e})\right);R_i(e)\right], \tag{4}$$

where $M_{i,e_b}(\bar{e})$ is the response matrix of the detector for mono-energetic X-rays, i is the index representing the layers, e_b is the index representing the energy bins, e is the total energy deposition created by γ/X-ray events, and A_{e_b} is the amplitude of the detector matrix elements of the reconstructed spectrum. Finally, $R_i(e)$ represents the detector response to the measured γ/X-ray spectrum.

This algorithm is embedded in the Root program[54] and was tested for two different cases: first for the case in which no prior information on the shape of the input γ/X-ray spectrum exists on which a model can rely (the *unconstrained* case) and second under the assumption that the shape of the γ/X-ray energy spectrum is estimated or known from, for example, PIC simulations or experimental data (the *constrained* case). Figure 8 illustrates the reconstructed amplitudes for γ/X-ray energies at 3 MeV, 8 MeV, 13 MeV, and 18 MeV, including the uncertainties for the constrained and unconstrained cases. The reconstruction works well in the constrained case, which uses a PIC2D-simulated γ/X-ray spectral shape, as depicted in blue in Fig. 8. Since all reconstructed data lie within an assumed uncertainty, a rough estimation for the achievable resolution can be deduced to be ~30%–40%. As expected, the unconstrained case gives a reconstruction of much lower quality.

The information provided by the CsI(Tl) spectrometers will support the results obtained from the gamma spectrometer. It is planned to install up to five of these rather compact CsI(Tl) spectrometers at variable positions inside the E1 target chamber at a safe distance from the laser interaction point (≳50 cm). A flexible arrangement of the individual CsI(Tl) detectors will optimize the quality of the reconstruction of the laser-induced γ/X-ray spectrum between ~5 MeV and ~12 MeV, where the expected γ-radiation amplitude for experiments with 10 PW lies. For a schematic view of the CsI(Tl) detector, see Fig. 7(c).

e. GeV electron spectrometer for E6. The diagnosis of ultra-relativistic electrons generated via LWFA is, without a doubt, one of the most important development tasks at ELI-NP. LWFA experiments in E6 are expected to produce electrons with an energy over 5 GeV.[55] A dipole magnet will be the main diagnostic for direct characterization of the electron beam energy spectrum. Owing to the stochastic nature of the electron generation, there are a few relevant beam parameters that can vary within a certain range.

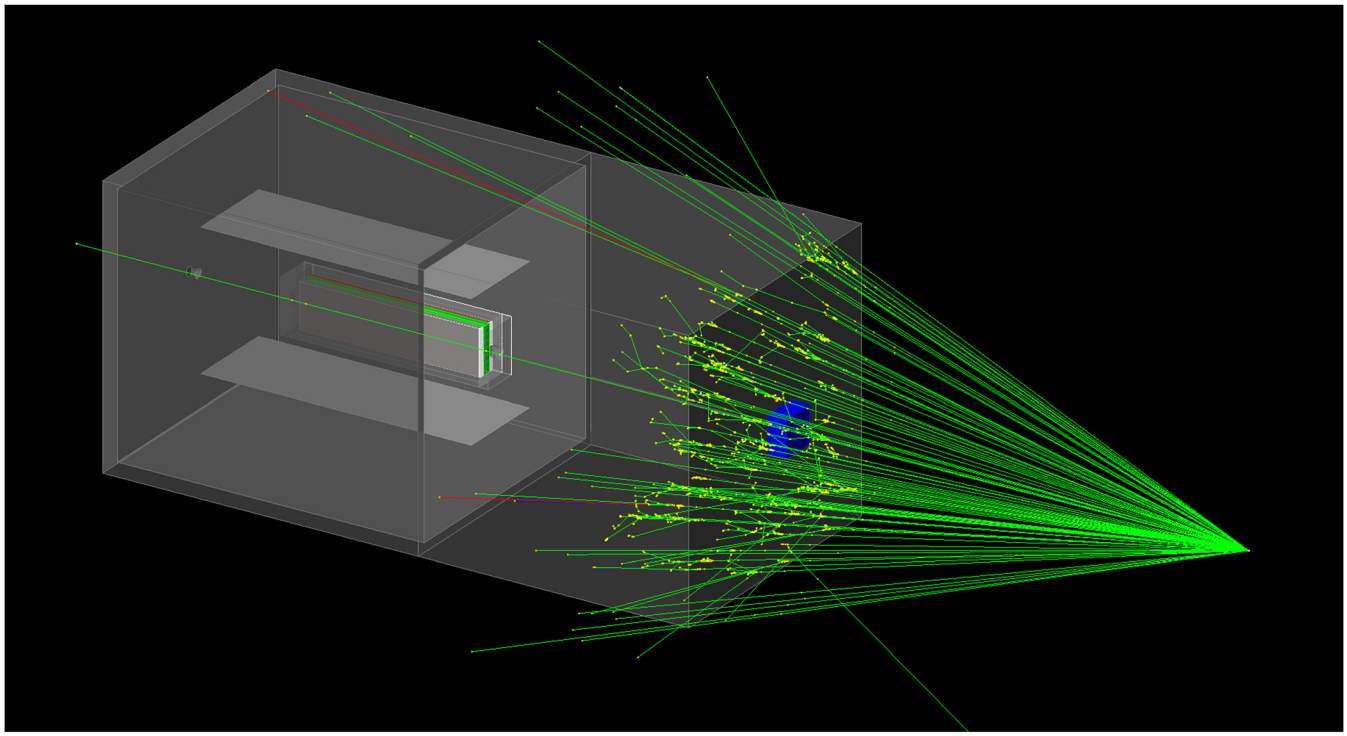

(a)

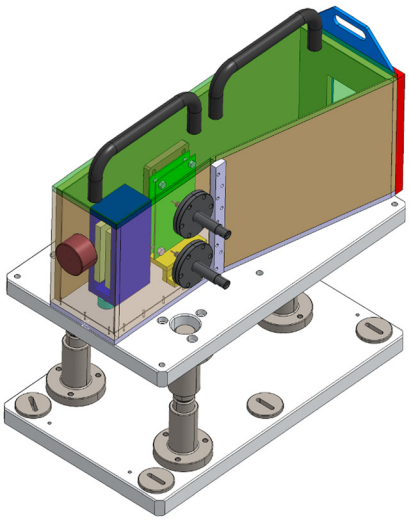

(b)

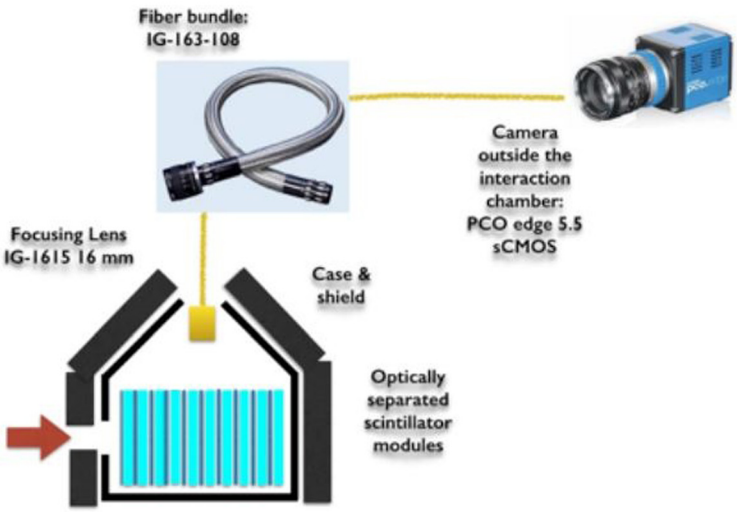

(c)

FIG. 7. (a) Geant4 simulation of the gamma spectrometer, showing γ rays (green lines) emitted from the target interacting with the front shielding (gray) of the spectrometer and with the Li converter target (solid blue), and generated secondary particles: electrons (red lines) and positrons (blue lines). The LANEX screens are horizontally aligned and depicted as light gray rectangles just below and above the parallel aligned separating magnets inside the detector. (b) Schematic 3D view of the Thomson parabola setup as planned for ELI-NP. The pinhole at the entry is in the middle of the cylinder depicted in purple. The two high-voltage feeds are shown in dark gray. The detector has an overall length of ~1 m. (c) Schematic cross-sectional view of the planned CsI(Tl) detector system. The beam entry is indicated by the red arrow. The scintillator elements are depicted in blue and encapsulated by a canvas of lead for shielding purposes. The attenuators between are shown as white stripes. The optical fiber cable feeding the camera is displayed at the top. The length of the detector is ~20 cm.

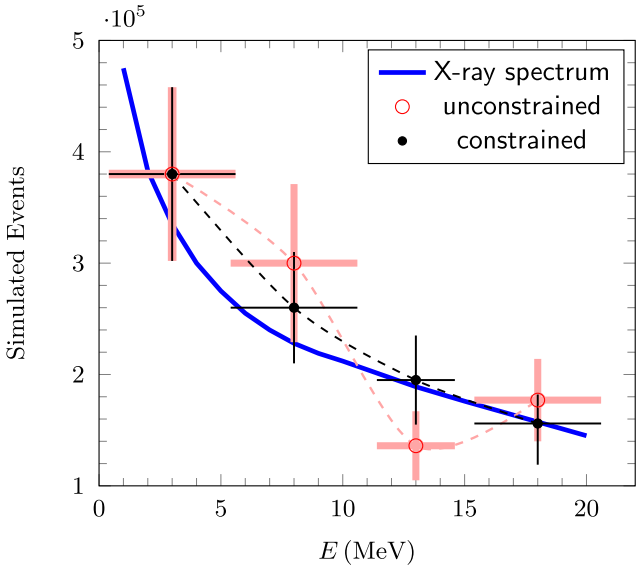

FIG. 8. Reconstruction of a γ/X-ray energy spectrum for the constrained (data shown by full black circles and uncertainties by thin black lines) and unconstrained cases (red open circles and thick pink lines) following Eq. (4). Note that for 3 MeV, the reconstructed data points are identical for both cases. The dashed lines represent the residuals of the reconstruction process and show that the quality of the constrained reconstruction is far superior to that of the unconstrained case.

These include, for instance, the electron beam energy spectrum, the beam pointing, and the beam divergence, which are most significant. A suitable design of the magnet and the relative beam diagnostic system needs to take these uncertainties into account. Therefore, the dipole magnet has been designed with a relatively large gap of 30 mm and with a magnetic field strength $|\mathbf{B}| \sim 1$ T. The dipole is 80 cm long, and the field in the center of the gap will be rather uniform, with a typical 2D super-Gaussian profile inside the gap. The dipole will be placed inside the interaction chamber, and the magnet will about 60 cm away from the primary target area in the gas cell. The typical electron beam pointing fluctuation about the laser axis and its divergence from a single-stage gas cell target are typically 3 mrad and 15 mrad, respectively.[56,57] This will correspond to a maximum variation of the position of the beam at the exit of the magnet gap of about ±4 mm and a beam radius of about 11 mm. Consequently, with a gap of 30 mm, the electron beam will not hit the chassis of the magnet in normal operation. In addition, a collimator can be placed in front of the entrance of the magnet to tailor the beam size if required. The detection system inside the detector consists of LANEX screens whose scintillation light will be collected by an imaging system and detected by a high-resolution CCD camera. The whole system will allow an electron energy resolution δE ranging from a few percent for hundreds of MeV to 10% for 5 GeV.

An additional dipole magnet with identical characteristics will be available in due course to be used outside the E6 chamber in conjunction with the internal one. This second detector will increase the resolution for high-energy electrons with energies above $E_e = 5$ GeV.

f. Passive detectors. Besides the aforementioned active detectors, passive detectors systems such as radiochromic film (RCF), Columbia Resin (CR-39), image plates, and activation plates will be used to support the commissioning measurements. Passive detectors are well-characterized diagnostic tools and have been successfully used in laser-driven ion acceleration experiments for over two decades. Although conceptually they are "simple" detectors, they require a dedicated design that is adapted to the experimental conditions arising from the unprecedented power of the ELI-NP laser. The activated radioactive exit channels permit deduction of the integral cross-section σ^{int} of γ/X-ray and proton-induced nuclear reactions with high precision in the offline analysis. For example, two γ-induced reactions on a probe of natural tantalum, ^{181}Ta, the only stable isotope of this element, lead to two radioactive daughter isotopes: ^{181}Ta$(\gamma,n)^{180}$Ta and ^{181}Ta$(\gamma,3n)^{178}$Ta. The created tantalum isotopes have half-lives $t_{1/2}(^{180}\text{Ta}) = 8.15$ h and $t_{1/2}(^{178}\text{Ta}) = 2.36$ h, and their decay results in a unique, very characteristic γ-decay pattern, which can be studied in an offline arrangement using HPGe detectors. The measured yield ratio allows the deduction of an estimate for the temperature k_BT of the initial γ/X-ray flash in the region between ~2 MeV and ~30 MeV, as demonstrated by Spohr *et al.*[58] In the same work, a C/Cu stack consisting of a 4 mm plastic foil and a 3.25 mm copper foil was used to induce the two reactions ^{12}C$(\gamma,n)^{11}$C and ^{63}Cu$(\gamma,n)^{62}$Cu, which lead to β^+ emission in both exit channels with half-lives $t_{1/2}(^{11}\text{C}) = 20.36$ min and $t_{1/2}(^{62}\text{Cu}) = 9.67$ min. The associated offline measurement reaction yield for the carbon and copper isotopes confirmed the measurement of the k_BT value of the γ/X-ray flash obtained from the tantalum data in the above-mentioned work. It is hoped that the activation method will support measurements with the CsI(Tl) spectrometer and the gamma spectrometer. Moreover, proton-induced activation of Cu filters via the reaction ^{63}Cu$(p,n)^{63}$Zn with $t_{1/2}(^{63}\text{Zn}) = 38.47$ m is a standard methodology in laser-driven experiments and is often applied together with a NaI(Tl) detector coincidence system with which the 511 keV photons created by the related positron annihilation can be measured. This very reaction was used to verify the highest kinetic energy obtained to date for laser-induced proton acceleration by Higginson *et al.*[26] The investigators were able to confirm kinetic proton energies $E_p \approx 100$ MeV. It is therefore mandatory to implement these established passive methods in the commissioning campaigns at ELI-NP.

Furthermore, passive detector systems made of stacks of RCF and CR-39 will be able to support the detection of protons with potential energies of up to 250 MeV and to discriminate well the cutoff point of the energy spectrum. Simulations for these stacked devices were undertaken with Geant4 and Srim[59] programs. For the calculations, a square section of the stack of 50 mm × 50 mm was assumed and a beam divergence of 30°. Energy calibrations for the response of the RCF stacks to low-energy protons were already undertaken experimentally with the 9 MV accelerator at IFIN-HH.[60] During the inaugural commissioning experiments, the RCF stack detector will be placed a few centimeters from the target and in front of the Thomson parabola spectrometer, thus capturing a large number of lower-lying protons in the first layers. The positioning of the stacks should be versatile, since progression to higher intensities I_0 could change the beam divergence. Their use in single-shot and sequential/multishot laser modes is also foreseen, and an assembly of motorized stages will allow multiple RCF stacks to be used.

g. Optical plasma probe. Optical probing systems will be available in the E1, E5, and E6 areas, to be used for the characterization of

the plasma electron density n_e. The probe is a pickup of the main laser pulse. Therefore, it will have a fundamental wavelength λ_0 between 814 nm and 825 nm and a pulse duration $\tau_{LP} \lesssim 22.5$ fs. Furthermore, λ_0 can be halved by a crystal to $\lambda \sim 410$ nm. This will allow the study of plasma electron densities ranging from $n_e = 10^{17}$ cm^{-3} to 10^{20} cm^{-3}. The presence of a delay line will also allow variation of the probing time from a few hundreds of picoseconds before the main laser pulse interacts with the target to a few nanoseconds after. The optical probe will be employed with diagnostics such as interferometry, shadowgraphy, schlieren, and polarimetry.

A summary of the detector systems used for the study of laser–matter interactions in E1, E5, and E6 is given in Table V (active detectors) and Table VI (passive detectors). The detector name and the radiation for which it is designed, as well as the highest detectable energy, are displayed in the first column. In the "Parameters" column, "OP" refers to the operating principle, $E_{p,\gamma}$ represents the maximum kinetic proton or γ energy and $\delta E_{p,\gamma}$ refers to their uncertainties; Ω_{geo} is the geometrical solid angle acceptance and $\Delta\Theta$ is the angular acceptance. Where possible, the expected total efficiency ε_{tot} is shown, given by $\varepsilon_{tot} = \Omega_{geo}\,\varepsilon_{int}$, with ε_{int} being the simulated intrinsic efficiency of the detector. "Dimensions" refers to the overall envelope dimension of the specific detector system, and "Weight" to the approximate weight of the detector. "Shielding" summarizes the shielding arrangements to be implemented for a specific detector device, derived from Geant4 simulations. "No." refers to the proposed number of detector devices of this kind to be implemented at an individual target station. Finally, "Readout" specifies the readout technology used.

2. Setup for E1 and E6

A rendered view of a potential experimental arrangement in the E1 target station is given in Fig. 9. The gamma spectrometer and the e^-–e^+ spectrometer are placed at 30° to the target normal, while the Thomson parabola to the left is looking at the direction of laser propagation. The CsI(Tl) detectors are not depicted. The inner dimensions of the reaction chamber are 4.0 m × 3.3 m × 1.8 m.

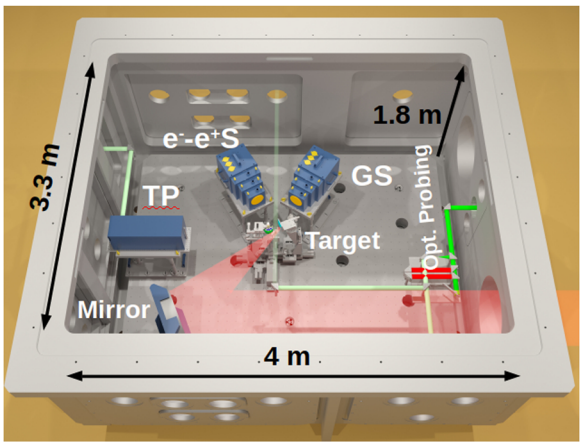

FIG. 9. Proposed setup of the diagnostic detectors for a typical commissioning experiment at E1, showing the envelope of the Thomson parabola (TP) in blue close to the left target wall, as well as the gamma spectrometer (GS) and the e^-–e^+ spectrometer (e^-–e^+S), which are placed facing the interaction point in the primary target in the vicinity of the middle of the chamber. The laser pulse envelope is shown in light red, with the focusing *f*/2.7 parabolic mirror on the lower left. The green (tube-) line indicates the light path associated with the optical plasma probing arrangement. The yellow circles on top of the gamma and e^-–e^+ spectrometers indicate the connecting points for the optical fibers to be used for the readout.

The E6 chamber will have the shape of a rectangular parallelepiped with the same spatial dimensions as the E1 chamber. The target will be a gas jet or a gas cell about 10 cm long. The interaction of the gas target with the long-focal-length laser beam will produce multi-GeV electrons, which will be diagnosed by a permanent dipole magnet and scintillator screens. The gas target will be probed by an optical probing system using a laser beam with a wavelength in the fundamental or second harmonic of the main laser and a pulse duration of ≲22.5 fs. Laser beam diagnostics will also be present to have a better understanding of the interaction processes. A laser beam bump will be placed at about 10–30 cm away from the exit of the gas cell and reflected off the main interaction chamber to stop the laser beam propagating further toward the chamber wall.

IV. HIGHLIGHTS OF THE INAUGURAL EXPERIMENTAL PROGRAM AT VEGA

ELI-NP will construct a γ-beam system called VEGA that will be able to provide γ-ray beams with energies up to 19.5 MeV and a high degree of linear polarization of >95%. The production of the quasi-monochromatic γ beam is based on the inverse Compton scattering process in which the laser light pulses are scattered off relativistic electron bunches. The VEGA system at ELI-NP will become one of the state-of-the-art facilities for delivering γ beams with photon spectral densities and bandwidths orders of magnitude better than current technology allows.

A versatile experimental research program is under preparation for the VEGA system. The experiments will focus on different aspects of photonuclear physics and aim to exploit to the full extent the unique performance characteristics of the VEGA system, such as the narrow bandwidth of the beams, their high brilliance, and their high degree of polarization. Different aspects of the γ-beam-related research program have been reviewed recently in a series of works.[6,61,62] In the following, several important studies within the scope of this research program are highlighted. They are related to different fields in photonuclear physics, such as NRF, photonuclear reactions, studies of nuclear resonances, and photo-fission research. NRF utilizes pencil-like, narrow-bandwidth, highly polarized γ beams with a spectral photon density of around 10^4 s^{-1} eV^{-1}. This enables NRF experiments with higher sensitivity and improved yield, and minimizes the mass of the targets, which, in most cases, will consist of very expensive, isotopically enriched materials. Thus, at ELI-NP, it will be possible to use targets made from only a few hundred milligrams of material, which opens an avenue for studies of less abundant isotopes, such as p-process nuclei or actinides. Note that, so far, there have been very few NRF studies in the actinide region, such as for ^{232}Th or ^{236,238}U.[63]

To perform these studies, the ELI-NP Array of Germanium Detectors (ELIADE)[64] is currently under construction at ELI-NP. It consists of eight HPGe clover detectors of TIGRESS type.[65] The detectors are arranged in two rings, each ring having two detectors in the vertical plane and two in the horizontal plane. Each clover detector consists of four encapsulated n-type HPGe crystals, which

are manufactured from a crystal with a diameter of 60 mm and a length of 90 mm. The outer surface of each crystal is tapered over 30 mm from the front of the crystal to allow close packing. The core contact has a diameter of 10 mm and a depth of 75 mm. Each crystal is divided into four quadrants and two lateral sections via an outer boron-implanted contact. Thus, nine signals are read for each crystal, resulting in 36 signals per detector and a total of 288 electronic channels for the HPGe array. Also, for the measurement of high-energy γ rays, bismuth germanate (BGO) scintillators will be mounted as back plugs to suppress background noise. Large $LaBr_3$(Ce) detectors can be mounted in positions at 45° with respect to the HPGe clover detectors. This arrangement will increase the overall efficiency of the array. As of Autumn 2019, all detectors and electronics have been delivered and tested at the ELI-NP premises. Mechanical support and the liquid nitrogen cooling systems of the array are under construction, and a data acquisition system (DAQ) has been implemented and tested. A 3D CAD view of ELIADE is presented in Fig. 10. In the shown configuration, the array will have an absolute γ-ray efficiency of ~6% and will enable coincidence measurements as well as serving as an excellent γ-ray polarimeter and thus providing opportunities for studies of γ-ray angular correlations.

For the commissioning NRF experiment, one considers the photoactivation measurement of ^{180}Ta.[6] An important part of the ELIADE research program concerns high-resolution studies of $E1$, $M1$, and $E2$ modes in the region below the neutron evaporation threshold of nuclei. It will be possible to distinguish and separate different excitations in the overlapping region of the pygmy dipole resonance (PDR), the giant dipole resonance (GDR), the magnetic dipole resonance (MDR), and the pygmy quadrupole resonance (PQR). The γ-ray efficiency of ELIADE will provide an opportunity to measure details of the γ-ray decay of such excitations, for example, the ground-state decay vs the decay to excited states. Such studies will inform theoretical models aimed at describing pygmy resonances in atomic nuclei. The experiments will be sensitive to weak branches of different excitation modes. For example, the electric dipole polarizability α_D is very sensitive to the low-lying $E1$ strength, and is correlated to the neutron skin thickness in a robust and less model-dependent manner.[66–69] These theories connect the slope of the symmetry term of the nuclear equation of state (EoS) to the neutron skin thickness. The polarizability α_D is related to the photoabsorption cross-section σ_{abs} by[70,71]

$$\alpha_D = \frac{\hbar c}{2\pi^2} \int_0^\infty \frac{\sigma_{abs}(E)}{E^2}\, dE, \tag{5}$$

where E denotes the excitation energy and σ_{abs} the absolute cross-section. Note that α_D depends strongly on the $E1$ strength at low energies. For the stable nucleus ^{208}Pb, the neutron skin thickness was extracted from the measured α_D.[72] Such experiments will be performed with higher sensitivity at the VEGA system with the ELIADE array.

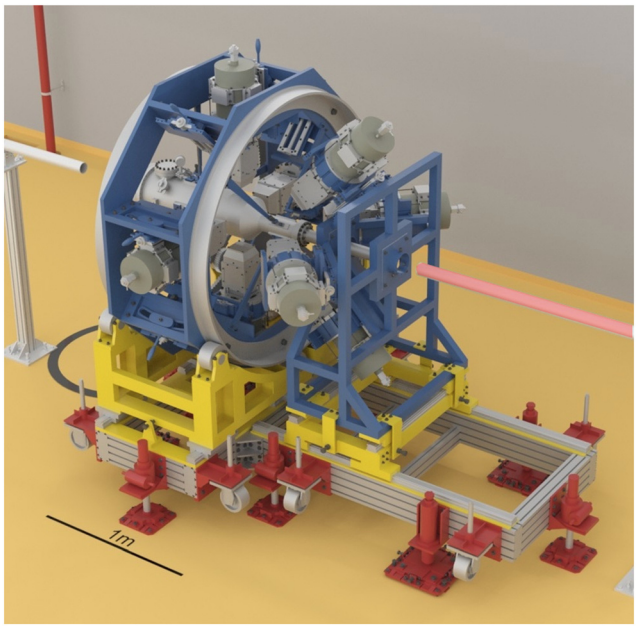

FIG. 10. A 3D CAD view of the ELIADE array with the HPGe detectors shown in gray. The supporting frame is shown in blue. The voids in the frame can be equipped with $LaBr_3$(Ce) detectors for selected experimental campaigns. The pipe for the incoming beam is shown in pink. Courtesy of A. Imreh.

A. Experiments above the particle evaporation threshold

An array of large-volume scintillation detectors consisting of 15 $LaBr_3$: Ce crystals (3 in. × 3 in.) coupled with Hamamatsu R11973 photomultiplier tubes (PMTs) and 19 $CeBr_3$ crystals (3 in. × 3 in.) coupled with Hamamatsu R6233 PMTs is under construction at ELI-NP. This array will be combined with 37 EJ301 liquid scintillator neutron detectors and 25 GS20 ^{6}Li glass detectors, called the ELI Gamma Above Neutron Threshold Gamma Neutron (ELIGANT-GN).[73,74] The detectors will be placed at backward angles, as demonstrated in the 3D CAD design of the array in Fig. 11. The $LaBr_3$(Ce) detectors are mounted on a frame 30 cm away from the target. The neutron detectors are mounted on movable mechanical structures, allowing a maximum distance of 1.5 m from the target, which is sufficient for the time-of-flight (ToF) separation of the neutrons. The array will provide the possibility for measurements of single and coincidence γ-ray events with the $LaBr_3$(Ce), single-neutron (n) events in the EJ301, and GS20 detectors and coincidence γ–n in the γ and neutron detectors. The first experiments will target the ground-state γ decay of the GDR and the PDR, as well as studies of two-step γ decay through low-lying states. These can be combined with measurements of the (γ, n) branch, providing precise data for the branching ratios. Detailed Geant4 simulations of the performance of the ELIGANT-GN array, a study of the response of the lanthanum bromide, and the EJ301 liquid scintillator detectors, as well as beam-time estimates, are provided in the work by Krzysiek *et al.*[74] Planned commissioning experiments address, for example, a study of the $E1$ strength of ^{208}Pb.[6,67,74,75]

Measurements of cross-sections of photoneutron reactions will be done with an array of 30 ^{3}He counters embedded in

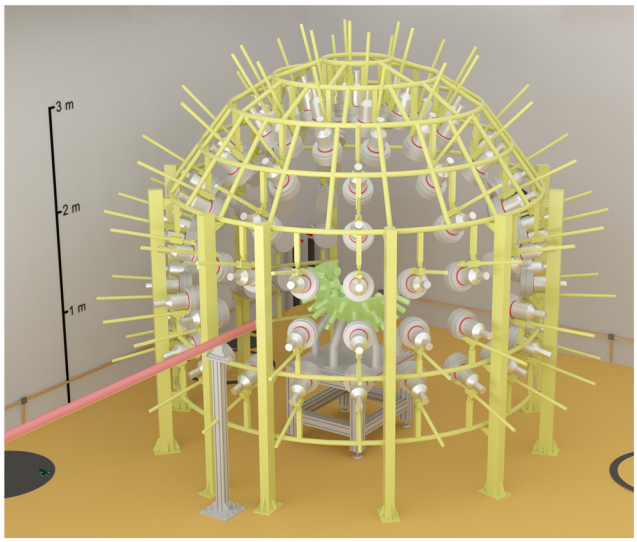

FIG. 11. A 3D CAD view of the ELIGANT-GN array. The lanthanide bromide detectors are mounted in the inner frame (green). They cover the bottom half of the full sphere angles and are placed inside the outer frame (yellow) supporting the neutron detectors. These detectors cover the upper half of the sphere and are depicted in gray (the small red circles show the junctions with the coupled PMTs). The beam pipe emerging from the lower left of the figure is shown in pink. Courtesy of A. Imreh.

polyethylene, which serves as a moderator for thermalization of the neutrons.[73] The array, which is called ELI Gamma Above Neutron Threshold Thermal Neutrons (ELIGANT-TN), is designed such that it has a flat efficiency of about 38% below E_n = 3 MeV and dropping to about 35% at higher energies up to 5 MeV. More than 90% of the neutron spectrum stays in the flat region, which allows cross-section measurements with an uncertainty <1%, as demonstrated in experiments with a similar device at the NewSubaru facility.[75] Furthermore, the average neutron energy can be extracted using the ring ratio method.[76] A commissioning study with ELIGANT-TN will be the measurement of the photodisintegration of ^{9}Be,[6] for which data from different measurements are in disagreement.[77–79] The experimental program at the VEGA system at ELI-NP aims further to also cover other aspects of photonuclear physics, such as photofission[80] and studies of photonuclear reactions that coincide with the emission of charged particles.[81] For realization of these experiments, different instruments will be available at ELI-NP. In particular, for photofission, two detector arrays are under construction, the ELI Bragg Ionization Chamber (ELI-BIC) and the ELI Thick Gas Electron Multiplier (ELITHGEM) arrays,[6,80] which will be used for measurements of photofission cross-sections and of mass, charge, angular, and kinetic energy distributions. Moreover, the occurrence of processes with very low cross-sections, such as transmission resonances,[82] highly asymmetric fission, clusterization phenomena, and triple fission, is foreseen.

The envisaged studies of charged particle photonuclear reactions are related to key nuclear astrophysics reactions, such as the ^{16}O(α, γ)^{12}C reaction. The physics case for these studies is discussed at length in Refs. 6 and 81. Two state-of-the-art instruments are under construction at ELI-NP: a time-projection chamber called the ELI Time Projection Chamber (ELITPC),[83,84] with a readout based on gas electron multiplier (GEM) technology, and a 4π array of silicon strip detectors called the ELI Silicon Strip Array (ELISSA).[81] In addition, an applied physics program for material characterization studies will be carried out, facilitating a dedicated slow-positron beamline named ELI Positron Source (ELIPS). A concise summary of the detector systems introduced in this section is given in Table VII. The notation in the "Parameters" column is the same as that in Table V, with the addition of f_{max} describing the maximum frequency a detector system can cope with, $\delta x_{p,\alpha}$ denoting the uncertainty in the determination of the lateral position for protons, and α and δt(FWHM) denoting the full width at half maximum of the time resolution.

B. Probing the microscopic structure of nuclear excitation modes at ELI-NP

With the unique possibilities provided by the VEGA system at ELI-NP, nuclear theory will have the opportunity to be informed by high-resolution data stemming from photon-induced excitations and reactions.

In this respect, one of the most exciting achievements of modern nuclear structure physics is the observation of two new excitation modes at low energy, namely, the PDR[85] and its higher-multipole extension the PQR,[86–88] both of which reveal novel aspects of the dynamics of isospin-asymmetric nuclear matter. In these findings, an enhanced electric dipole or quadrupole strength, respectively resembling a resonance structure below or close to the neutron emission threshold, was detected as a standard feature of stable and unstable nuclei with neutron excess. It was associated with oscillations of a small outer layer of neutron-rich nuclear matter with respect to the isospin-symmetric nuclear core.

From systematic studies of nuclear isotonic and isotopic chains, a correlation of PDR and PQR strengths and nuclear-skin thickness was found, and the connection of PDR and PQR to oscillations of weakly bound nucleons at the nuclear surface was further confirmed by analysis of nuclear ground states and neutron and proton transition densities.[86,89,90]

During the last few years, the PDR has been the subject of many experimental and theoretical investigations.[85,91,92] However, most theoretical studies of the PDR have been limited to the quasiparticle random-phase approximation (QRPA), which cannot explain in detail the experimental data on low-energy dipole excitations and the PDR fragmentation pattern. For that purpose, an extended approach based on energy density functional (EDF) plus three-phonon quasiparticle phonon model (QPM) theory[89,90,93] has been developed that explicitly accounts for the interactions beyond particle–hole (p–h) configurations. In particular, the QPM formalism allows for further expansion of QRPA p–h excitations to multiparticle-multihole states in terms of coupling between quasiparticles and phonons.[94] Thus, for spherical even–even nuclei, the model Hamiltonian is diagonalized on an orthonormal set of wave functions constructed from one-, two-, and three-phonon configurations:[95]

TABLE VII. Summary of detector systems related to the VEGA system in the areas E3, E7, E8, and E9 at ELI-NP.

Detector and purpose	Area	Parameters
ELIADE: For γ rays (E_γ)	E8	OP: γ Detection with eight segmented HPGe detectors (32 crystals, 256 segments) and four $CeBr_3$ detectors; E_γ = 40 keV–10 MeV; δE_γ = 0.12%–0.3%; $f_{max} \sim 100$ Hz per segment; $\Omega_{geo} = 5$ sr; $\Omega_{tot}(1.3\ MeV) = 6\%$. Readout: Electronic digitizers
ELIGANT-GN: For γ rays (E_γ) and neutron detection	E9	OP: 15 $LaBr_3$:Ce detectors, 19 $CeBr_3$ detectors, 37 EJ-301 liquid scintillators, and 25 GS20 Li-glass detectors; $E_\gamma \lesssim 20$ MeV; $\Omega^n_{geo} = 1.72$ sr; $\Omega^\gamma_{geo} = 1.36$ sr; $\Omega_{tot}(10\ MeV) \sim 1\%$ for $LaBr_3$; $\Omega_{tot}(5\ MeV) \sim 3\%$ for EJ-301; $\Omega_{tot}(250\ keV) \sim 0.3\%$ for GS20. Readout: Electronic digitizers
ELIGANT-TN: For thermal neutrons	E9	OP: 28 ^{3}He detectors; E_n = thermal, δE_n = given by ring method; $\Omega_{geo} \sim 4\pi$ sr; $\Omega_{tot}(3\ MeV) \lesssim 38\%$. Readout: Electronic digitizers
ELISSA: For protons and α particles	E8	OP: 35 X3 DSSSD detectors (barrel) and 8 QQQ3 DSSSD (endcap); E_p = 100 keV–10 MeV; E_α = 100 keV–30 MeV; $\delta E_{p,\alpha}$ = 40 keV (front)–80 keV (back); $\Omega_{geo} = 10$ sr; $\Omega_{tot} \sim 80\%$ in total range. Readout: Analogue
ELITPC: For protons and α particles	E7	OP: Determination of tracks in gas-filled chamber; $E_p(100\ mbar) \gtrsim 85$ keV; $\delta x_{p,\alpha} \lesssim 0.4$ mm. Readout: Digital
ELI-BIC: For fission fragments	E7	OP: Four Bragg twin ionization chambers with Frisch grids and two ΔE–E, Si-strip detector telescopes. Readout: Digital
ELITHGEM: For fission fragments	E7	OP: 12 thick gas electron multipliers, $f_{max} \lesssim 2$ kHz; $\Omega_{geo} = 10$ sr; $\delta\Theta \lesssim 5^\circ$. Readout: Time-to-digital converter (TDC), digital
ELIPS: For E and t spectra of annihilation γ rays, e^+ lifetimes, Doppler shift, Auger electrons	E3	OP: Four HPGe detectors and BaF_2 detector; $\delta E_\gamma(511\ keV) \lesssim 1.2$ keV; $f_{max} \lesssim$ 20 kHz per detector; $\delta t(FWHM) = 250$ ps. Readout: Digital

$$\Psi_\nu(JM) = \Bigg\{ \sum_i R_i(J\nu) Q^+_{JMi} + \sum_{\substack{\lambda_1 i_1 \\ \lambda_2 i_2}} P^{\lambda_1 i_1}_{\lambda_2 i_2}(J\nu) [Q^+_{\lambda_1\mu_1 i_1} \otimes Q^+_{\lambda_2\mu_2 i_2}]_{JM} + \sum_{\substack{\lambda_1 i_1 \lambda_2 i_2 \\ \lambda_3 i_3 I}} T^{\lambda_1 i_1 \lambda_2 i_2 I}_{\lambda_3 i_3}(J\nu) [\,[Q^+_{\lambda_1\mu_1 i_1} \otimes Q^+_{\lambda_2\mu_2 i_2}]_{IK} \otimes Q^+_{\lambda_3\mu_3 i_3}]_{JM} \Bigg\} \Psi_0, \tag{6}$$

where R, P, and T are unknown amplitudes and ν labels the number of the excited state. The electromagnetic transition matrix elements are calculated for transition operators, including the interaction of quasiparticles and phonons,[96] where exact commutation relations are implemented, which is a necessary condition to satisfy the Pauli principle.

Presently, the above is one of the most elaborated theoretical method allowing a unified description of low-energy single- and multiple-phonon states and the GDR. Besides, an important advantage of QPM compared with other methods involving quasiparticle–phonon coupling is the use of large configuration spaces,[97] which is of great importance for quantitative descriptions and predictions of nuclear data.

Spectral distributions of low-energy $E1$ and $M1$ strengths below the neutron threshold in ^{206}Pb ($S_n = 8.087$ MeV) have recently been studied,[97] and the results are shown in Fig. 12. It is found that the low-energy $E1$ and $M1$ strength is strongly fragmented. In the $E1$ case, this is due to the interaction of the p–h QRPA states from the PDR and those from the GDR tail and also interactions with multiphonon configurations with different spin and parity. A detailed EDF + QPM analysis of the $E1$ transition matrix elements strongly suggests that the PDR or the neutron skin oscillations dominate the distribution of the dipole strength up to about 7 MeV, at which point the tail of the GDR starts to make an important contribution.[97] Overall, the PDR and the GDR account respectively for about 77% and 12% of the $E1$ strength below the neutron separation energy in ^{206}Pb. Also significant is the impact of multiphonon states on the total $E1$ strength and, to a lesser extent, the $M1$ strength.

Furthermore, from recent studies of the microscopic structure of low-energy quadrupole states and the PQR mode in tin isotopes, it has been found that essential information for different nuclear excitation counterparts can be derived from ground- and excited-state branching ratios.[98] Theoretical and experimental observations show that branching ratios can also provide useful information on the collectivity of the excited nuclear states. In addition, they serve as a sensitive indicator for the small components of nuclear state vectors that are difficult to detect by other observables.[98]

According to theoretical observations, the existence of PDR might have a large impact on neutron capture reaction cross-sections[97,99,100] contributing to the nucleosynthesis. One common conclusion from these studies is that the nuclear excitations below the neutron threshold have complex behavior that is influenced by the competition between static and dynamic effects. This involves the coupling of the PDR p–h excitations with multiparticle–multihole states related to core polarization. The latter leads to redistribution and fragmentation of the low-energy electrical dipole strength (see Fig. 12), which can significantly affect radiative capture cross-sections

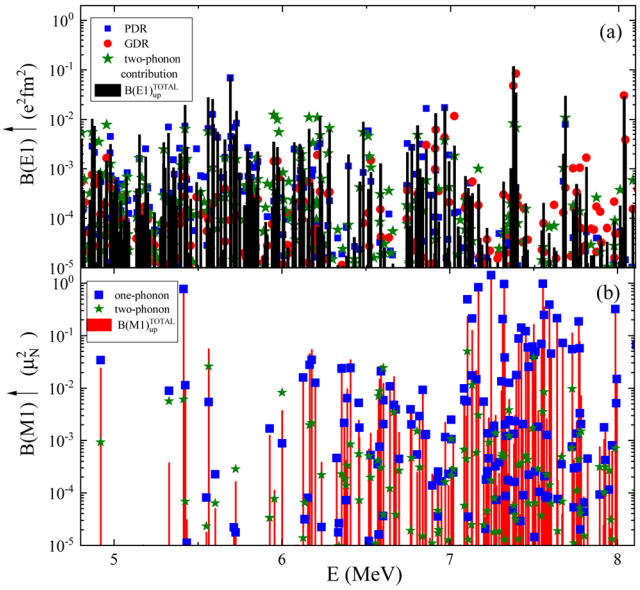

FIG. 12. Low-energy electric dipole (*E*1) strength (a) and magnetic dipole (*M*1) strength (b) distributions for ^{206}Pb. Different counterparts of the transition matrix elements related to (a) PDR, GDR, and multiphonon contributions to the total *E*1 strength and (b) single-phonon and multiphonon contributions to the total *M*1 strength, obtained from the three-phonon EDF + QPM approach, are shown.

at astrophysical energies.[97,99,100] Therefore, the correct determination of the radiative capture reaction rates at astrophysical energies requires very precise experimental measurements and elaborate theoretical calculations of nuclear spectral functions up to GDR energies. All this can be achieved at the coming ELI-NP facility with the detector systems described in the previous section.

C. Summary of the inaugural experimental program at the VEGA system

The VEGA system at ELI-NP will allow the study of different photonuclear reactions of scientific interest, such as activation and (γ, γ') reactions, which can be below and above the neutron evaporation threshold. Moreover, photodisintegration reactions and photofission can be investigated, as well as nuclear excitation modes, to enhance theoretical understanding of the PDR and the GDR. The physics program covers a wide range of topics, which are of general interest to the whole community.

V. LASER-BASED PRODUCTION AND CHARACTERIZATION OF γ-PHOTON BEAMS

ELI-NP will open up a gamut of experimental avenues for the exploration of high-energy and high-intensity γ-radiation-induced physics in the future. With the HPLS at ELI-NP, two methods can be used for the generation of high-energy γ rays with hitherto unmatched experimental intensity. First, one can facilitate inverse Compton scattering of the initial laser pulse by a relativistic electron beam provided by a LINAC to be installed as has already been demonstrated, for example, in Refs. 101 and 102. The VEGA system at ELI-NP can provide γ rays by this mechanism with a spectral density of the order of 10^4 s^{-1} eV^{-1}, reaching a maximum energy E_γ of up to 19.5 MeV. An alternative method is the use of the bremsstrahlung process as induced by intense relativistic electron beams impacting on a high-Z nucleus used as a radiator. A LINAC can provide the electron beam for this process, or a plasma-based accelerator facilitating the LWFA process can be used.[29,103–106] For example, the Production and Photoexcitation of Isomers Experiment (PPEx) in the E7 area of ELI-NP uses the electrons generated from LWFA to produce γ rays by bremsstrahlung.[107] The γ rays with energies in the region of the GDR (15–30 MeV) can be used to study various nuclear interactions for medical applications as well as astrophysical phenomena.[108,109]

A. The all-optical Compton γ-ray source at ELI-NP

Facilitation of the inverse Compton scattering process requires good synchronization between the laser pulse and the electron beam to optimize the γ-ray yield, especially for a tightly focused laser pulse.[57] Meanwhile, although bremsstrahlung is much easier to obtain, the related cross-section saturates for highly energetic incident electrons, and therefore the γ-ray yield is limited.[110] To solve these problems, an all-optical Compton γ-ray source was proposed.[111] In this approach, the relativistic electron beam is produced via LWFA and undergoes Compton backscattering from the same laser pulse, which is reflected from a plasma mirror naturally created in a solid target. X-ray pulses of a few hundred keV with a 10^4-fold increase in brightness compared with a Compton-based source using a conventional accelerator can be achieved in this way.

The laser intensities of the processes are currently limited to $0.04 \lesssim a_0 \lesssim 2$.[111,112] With the upcoming HPLS at ELI-NP, higher values of $a_0 = 10$–100 can be obtained. A simple modification can be made to the PPEx experiment to generate an all-optical Compton γ-ray source where a bremsstrahlung target is used as a plasma mirror. The laser pulse forms a concave shape on the target surface owing to the strong laser radiation pressure. This concave surface then acts as a focusing mirror to focus the back-reflected laser pulse to a spot size of a few laser wavelengths, and thus the laser intensity will be strongly increased.[113,114] A tightly focused laser pulse with intensity up to the order of $I_0 \sim 10^{22}$ W cm^{-2} may be obtained if the initial laser pulse reaches an intensity of the order of $I_0 \sim 10^{21}$ W cm^{-2}. During the collision of the laser pulse with the electron beam, radiation reaction (RR) will take place and convert a large portion of electron energy into γ rays.[115,116]

Preliminary estimations of the γ-ray generation have been performed using the two-dimensional (2D) PIC code Epoch,[27] in which LWFA is responsible for producing the relativistic electron beam from an underdense plasma. In the PIC simulation, a thin aluminum foil of 10 μm was positioned close to the exit of the gas jet to act as a plasma mirror. The back-reflected laser pulse propagating from the plasma mirror collides with the electrons to generate energetic γ rays. The so-called stochastic model of radiation emission is implemented in this simulation. To save computational time, this model is activated just before the mathematical treatment of the collision sets in. A detail analysis of this scheme is presented in Ref. 117. Two collimated γ rays from the nonlinear Compton backscattering and bremsstrahlung with peak brilliances of $n_{\gamma,1} = 6.7 \times 10^{20}$ s^{-1} mm^{-2} mrad^{-2} (0.1% BW)$^{-1}$ and

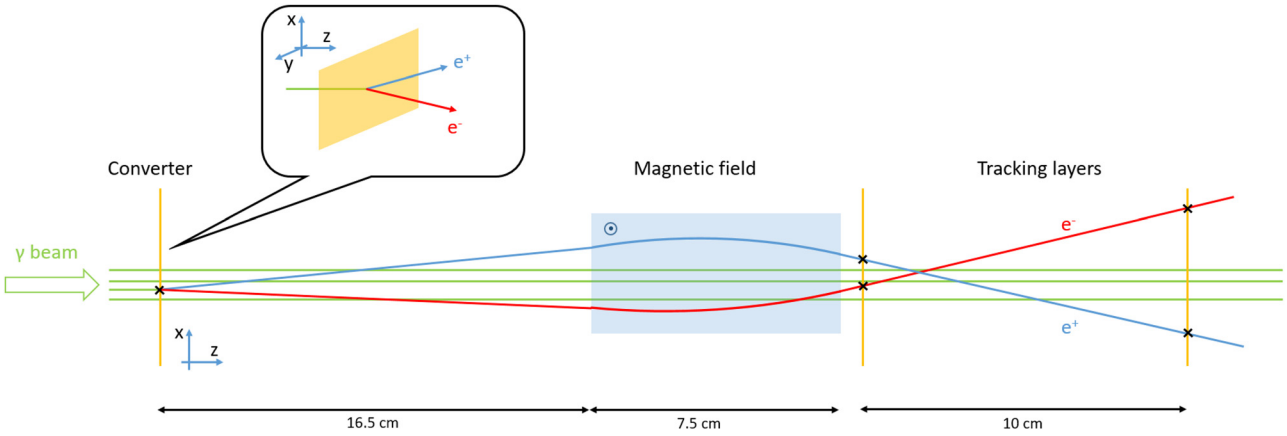

FIG. 13. The Gamma Polari-Calorimeter (GPC) design relies on the beam interacting with a converter material to produce electron–positron pairs. Both of these particles are measured using a combination of a magnetic field and pixelated position-sensitive detectors. The black crosses on the sensitive elements represent the input data that feed the reconstruction algorithm.

$n_{\gamma,2} = 2.1 \times 10^{16}$ s^{-1} mm^{-2} mrad^{-2} (0.1% BW)$^{-1}$ at 15 MeV are feasible by using just one 1 PW laser pulse.

B. The Gamma Polari-Calorimeter (GPC)

One of the research and development concerns of the group working on fundamental physics with combined laser and γ beams is the development of the Gamma Polari-Calorimeter (GPC), an instrument aimed at measuring both the energy and the degree of polarization of incoming γ rays. The specifics of the ELI-NP experiments, such as RR and vacuum birefringence measurements,[118] require measurements of both of these quantities using the same sample of photons to be able to reveal the dependence of the degree of polarization on the energy for a broadband γ beam. To accommodate the energy range between 100 MeV and 2 GeV,[119] the design of the proposed detector consists of a converter material in which some of the incoming photons are converted into electron–positron pairs, which are then tracked in a magnetic field using a thin, pixelated silicon detector array, as depicted in Fig. 13.

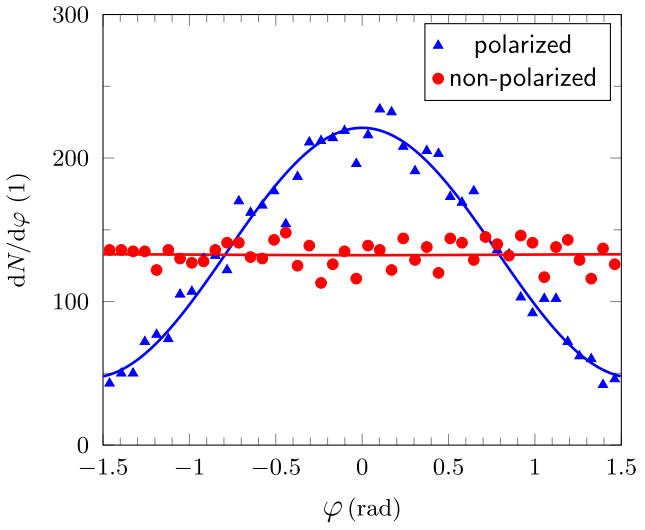

FIG. 14. Simulation of the azimuthal angle of the pair creation plane for a 1 GeV γ beam. Modulation of the cross-section in the linearly polarized case (blue triangles) is clearly emphasized compared with the non-polarized beam case (red circles).

The pair creation cross-section is modulated with the azimuthal angle φ of the pair creation plane, according to the following relation:[120]

$$\frac{dN_{e^+e^-}}{d\varphi} = N_0 (1 + AP_\ell \cos 2\varphi), \tag{7}$$

where P_ℓ is the degree of linear polarization of the beam, A represents the analyzing power of the setup, and N_0 is the cross-section of the process, making the detector sensitive to the γ-beam polarization angle.

The design involves pixelated silicon tracking layers and a magnetic field to reconstruct the electron and positron trajectories to obtain the 4-momenta of these particles. The azimuthal angle of the pair creation plane provides information on the degree of polarization of the beam, whereas the sum of the two 4-momenta provides the energy of the incoming high-energy photon. The momenta along directions perpendicular to that of beam propagation can be used for the measurement of the degree of linear polarization of the incoming beam, using the modulation of the cross-section with the angle φ.

Recent work has focused on numerical simulations and testing a GPC prototype without a magnetic field for the tracking of cosmic muons. Numerical simulations suggest that the energy resolution is below 7% for 1 GeV photons when considering a magnetic field strength of 1 T and just one reconstructed photon per pulse. Differences between nonpolarized and linearly polarized beams are shown in Fig. 14, which depicts the distribution of the angle of the pair creation plane for each of the two cases. Fitting the data to a cosine yields the amplitude of the modulation, with the analyzing power being $A = 0.65 \pm 0.02$ in these simulations. Moving to 10^3 incident photons on the detector for each shot, the energy resolution at 1 GeV is less than 8.5%, while the analyzing power is above 0.4. Although these simulations assume a perfectly uniform magnetic field, which is

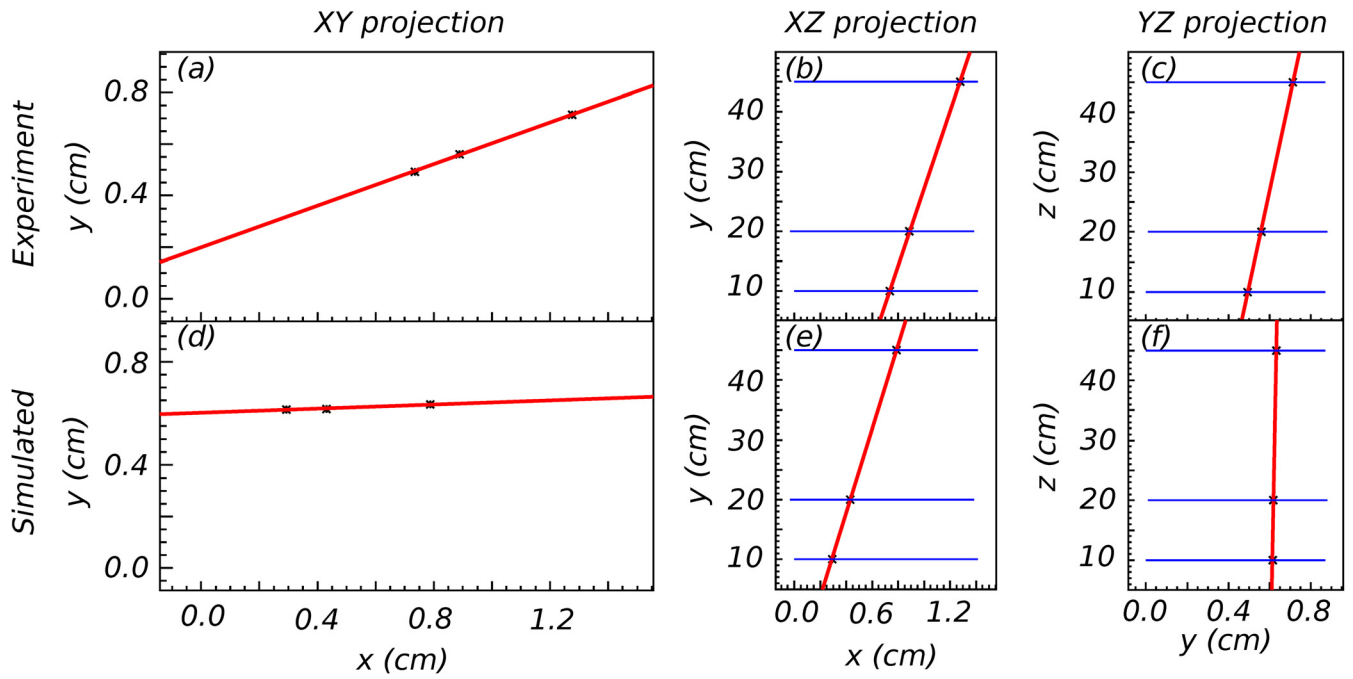

FIG. 15. Projections of cosmic muon trajectories in the detector volume. Experimental data is shown in (a)–(c) and simulated muon trajectories are displayed in (d)–(f) showing the projections of the trajectories on the *xy*, *xz*, and *yz* planes.

unrealistic in experimental practice, design studies to simulate a realistic Halbach array of rare-earth magnets using the Comsol software package yielded nearly identical results.

Currently, a prototype of the GPC detector without the application of a magnetic field is being used to validate the electronics and DAQ software with high-energy charged particles. The detector records cosmic muons that cross all three pixelated silicon layers, and real events are being compared with Geant4[42,53] simulations. The straight trajectories of cosmic muons can help correct detector misalignment, since systematic shifts of the silicon layers of the order of tens of micrometers can have a significant impact on the energy resolution. Cosmic muons are measured to validate the numerical simulations and to compensate for these misalignments. Figure 15 presents two events, a real event as taken from an experiment with the GPC prototype [Figs. 15(a)–15(c)] and one simulated event [Figs. 15(d)–15(f)]. The straight trajectories in the experimental data [Figs. 15(a)–Figs. 15(c)] have been obtained after misalignment corrections. The magnetic field will be provided by a Halbach array of permanent magnets, enabling the prototype to perform muon spectrometry as well as calorimetry and polarimetry of GeV γ rays. This magnet will bend the trajectories in the *xy* projection to make it possible to measure the charged particle momentum.

VI. CONCLUSIONS

We have started implementation at the Extreme Light Infrastructure for Nuclear Physics (ELI-NP), and the first experiments on the laser system will be undertaken in early 2020. The facilities at ELI-NP are unique and original in terms of having an ultraintense high-power laser system and a high-brilliance γ-beam system to offer to the community of nuclear physicists around the world. In summary, the main features of the systems are as follows:

1. A high-power laser system (HPLS) consisting of two 10 PW beams will deliver a laser pulse with E_{LP} = 150–225 J in each of the arms during a laser pulse duration of τ_{LP} = 15–22.5 fs and in a wavelength region of λ_0 = 814–825 nm. This leads to a maximum focal spot intensity $I_0 \sim 10^{23}$ W cm^{-2}. The laser system can also deliver lower powers at 100 TW and 1 PW. The flexibility of the HPLS at ELI-NP is further underpinned by five different experimental target areas, each having its own customized chamber. A laser power of >10 PW has already been demonstrated in Spring 2019.
2. The Variable-Energy Gamma Ray (VEGA) system at ELI-NP can deliver monoenergetic γ rays with up to 19.5 MeV, which can be extracted and directed to experimental target areas equipped with a variety of 12 different detector systems with distinct functionalities and widely changing sizes. The basic performance parameters are a photon density of $\sim 10^4$ s^{-1} eV^{-1}, with a high degree of linear polarization of >95%.
3. Various extreme states in gases, solids, and plasmas will be created using the above beams to study new regimes of nuclear and plasma physics. The flexibility of the system will allow combinations of any of the above beams to design unique and original experiments such as nonlinear quantum electrodynamics (QED), vacuum birefringence, relativistic induced transparency (RIT), nuclear resonance fluorescence (NRF), photoactivation, photonuclear reactions, and photofission.

ELI-NP is an international user facility with a key mission to allow access to academic and industrial user communities. Experiments with the HPLS and VEGA system will hopefully lead to innovative and

unique experiments. The ELI-NP group, which now consists of more than 300 scientists and technical support staff, will guide the external user programs. Part of the Technical Design Report (TDR) will be reflected in the commissioning experiments, which are approved by the International Scientific Advisory Board (ISAB) of ELI-NP. Altogether, starting from 2020, ELI-NP will hopefully enable new discoveries and the emergence of new disciplines in research, such as nuclear photonics and novel applications, which may have a large societal impact.

ACKNOWLEDGMENTS

The contribution of the entire ELI-NP team and collaborators to the project implementation is gratefully acknowledged, especially the help of A. Imreh in creating the complex 3D figures. The work has been supported by Extreme Light Infrastructure Nuclear Physics Phase II, a project co-financed by the Romanian Government and the European Union through the European Regional Development Fund and the Competitiveness Operational Programme (No. 1/07.07.2016, COP, ID 1334).

NOMENCLATURE

CE	Coulomb explosion
CP	circular polarization
CPA	chirped pulse amplification
CR-39	Columbia Resin
DAQ	data acquisition system
EDF	energy density functional
ELIADE	ELI-NP Array of Germanium Detectors
ELI-BIC	ELI Bragg Ionization Chamber
ELIGANT	ELI Gamma Above Neutron Threshold
ELIGANT-GN	ELI Gamma Above Neutron Threshold Gamma Neutron
ELIGANT-TN	ELI Gamma Above Neutron Threshold Thermal Neutrons
ELI-NP	Extreme Light Infrastructure for Nuclear Physics
ELIPS	ELI Positron Source
ELISSA	ELI Silicon Strip Array
ELITHGEM	ELI Thick Gas Electron Multiplier
ELITPC	ELI Time Projection Chamber
EMP	electromagnetic pulse
GDR	giant dipole resonance
GEM	gas electron multiplier
GPC	Gamma Polari-Calorimeter
HB	hole boring
HPGe	high-purity germanium (detectors)
HPLS	high-power laser system
LBTS	laser beam transport system
LIDT	laser-induced damage threshold
LINAC	linear accelerator
LS	light sail
LWFA	laser wakefield acceleration
MCP	multichannel plate
MDR	magnetic dipole resonance
NRF	nuclear resonance fluorescence
OPCPA	optical parametric chirped-pulse amplification
PDR	pygmy dipole resonance
PIC	particle-in-cell
PMT	photomultiplier tube
PPEx	Production and Photoexcitation of Isomers Experiment
PQR	pygmy quadrupole resonance
QED	quantum electrodynamics
QPM	quasiparticle phonon model
QRPA	quasiparticle random-phase approximation
RCF	radiochromic film
RIT	relativistic induced transparency
RPDA	radiation-pressure-dominated acceleration
RR	radiation reaction
S/N	signal-to-noise ratio
TDR	Technical Design Report
TNSA	target normal sheath acceleration
VEGA	Variable-Energy Gamma Ray

REFERENCES

[1]D. Strickland and G. Mourou, "Compression of amplified chirped optical pulses," Opt. Commun. **56**(3), 219–221 (1985).

[2]G. A. Mourou, "Nobel lecture: Extreme light physics and application," Rev. Mod. Phys. **91**, 030501 (2019).

[3]G. A. Mourou, T. Tajima, and S. V. Bulanov, "Optics in the relativistic regime," Rev. Mod. Phys. **78**, 309–371 (2006).

[4]N. V. Zamfir, "Nuclear physics with 10 PW laser beams at extreme light infrastructure-nuclear physics (ELI-NP)," Eur. Phys. J. Spec. Top. **223**, 1221–1227 (2014).

[5]S. Gales, D. L. Balabanski, F. Negoita, O. Tesileanu, C. A. Ur, D. Ursescu, and N. V. Zamfir, "New frontiers in nuclear physics with high-power lasers and brilliant monochromatic gamma beams," Phys. Scr. **91**(9), 093004 (2016).

[6]S. Gales, K. A. Tanaka, D. L. Balabanski, F. Negoita, D. Stutman, O. Tesileanu, C. A. Ur, D. Ursescu, A. Andrei, S. Ataman, M. O. Cernaianu, L. D'Alessi, I. Dancus, B. Diaconescu, N. Djourelov, D. Filipescu, P. Ghenuche, D. G. Ghita, C. Matei, K. Seto, M. Zeng, and N. V. Zamfir, "The extreme light infrastructure-nuclear physics (ELI-NP) facility: New horizons in physics with 10 PW ultra-intense lasers and 20 MeV brilliant gamma beams," Rep. Prog. Phys. **81**(9), 094301 (2018).

[7]The ELI-Nuclear Physics Working Groups, The White Book of ELI Nuclear Physics, 2010, URL: https://www.eli-np.ro/whitebook.php.

[8]Romanian Business News - ACTMedia, Magurele laser system reaches 10 PW; project manager calls it dream come true, 2019, URL: https://actmedia.eu/daily/magurele-laser-system-reaches-10pw-project-manager-calls-it-dream-come-true/80033.

[9]I. Dancus *et al.* (unpublished).

[10]K. W. D. Ledingham and W. Galster, "Laser-driven particle and photon beams and some applications," New J. Phys. **12**(4), 045005 (2010).

[11]A. Macchi, M. Borghesi, and M. Passoni, "Ion acceleration by superintense laser-plasma interaction," Rev. Mod. Phys. **85**, 751–793 (2013).

[12]S. Weber, S. Bechet, S. Borneis, L. Brabec, M. Bučka, E. Chacon-Golcher, M. Ciappina, M. DeMarco, A. Fajstavr, K. Falk, E.-R. Garcia, J. Grosz, Y.-J. Gu, J.-C. Hernandez, M. Holec, P. Janečka, M. Jantač, M. Jirka, H. Kadlecova, D. Khikhlukha, O. Klimo, G. Korn, D. Kramer, D. Kumar, T. Lastovička, P. Lutoslawski, L. Morejon, V. Olšovcová, M. Rajdl, O. Renner, B. Rus, S. Singh, M. Šmid, M. Sokol, R. Versaci, R. Vrána, M. Vranic, J. Vyskočil, A. Wolf, and Q. Yu, "P3: An installation for high-energy density plasma physics and ultra-high intensity laser–matter interaction at ELI-Beamlines," Matter Radiat. Extremes **2**(4), 149–176 (2017), exported from https://app.dimensions.ai on 05 February 2019.

[13]F. Negoita, M. Roth, P. Thirolf, S. Tudisco, F. Hannachi, S. Moustaizis, I. Pomerantz, P. McKenna, J. Fuchs, K. M. Spohr, G. Acbas, A. Anzalone, P. Audebert, S. Balascuta, F. Cappuzzello, M. Cernaianu, S. Chen, I. Dancus, R. Freeman, and N.

V. Zamfir, "Laser driven nuclear physics at ELI-NP," Rom. Rep. Phys. **68**, S37 (2016).
[14]J. Fuchs, P. Antici, E. d'Humières, E. Lefebvre, M. Borghesi, E. Brambrink, C. A. Cecchetti, M. Kaluza, V. Malka, M. Manclossi, S. Meyroneinc, P. Mora, J. Schreiber, T. Toncian, H. Pépin, and P. Audebert, "Laser-driven proton scaling laws and new paths towards energy increase," Nat. Phys. **2**, 48–54 (2006).
[15]J. M. Dawson, "Particle simulation of plasmas," Rev. Mod. Phys. **55**, 403–447 (1983).
[16]T. Z. Esirkepov, M. Borghesi, S. V. Bulanov, G. A. Mourou, and T. Tajima, "Highly efficient relativistic-ion generation in the laser-piston regime," Phys. Rev. Lett. **92**, 175003 (2004).
[17]V. Veksler, "Coherent principle of acceleration of charged particles," Proc. Symp. CERN **1**, 80 (1956).
[18]H. Daido, M. Nishiuchi, and A. S. Pirozhkov, "Review of laser-driven ion sources and their applications," Rep. Prog. Phys. **75**(5), 056401 (2012).
[19]S. C. Wilks, A. B. Langdon, T. E. Cowan, M. Roth, M. Singh, S. Hatchett, M. H. Key, D. Pennington, A. MacKinnon, and R. A. Snavely, "Energetic proton generation in ultra-intense laser-solid interactions," Phys. Plasmas **8**(2), 542–549 (2001).
[20]S. Bulanov, T. Esirkepov, V. Khoroshkov, A. Kuznetsov, and F. Pegoraro, "Oncological hadrontherapy with laser ion accelerators," Phys. Lett. A **299**(2), 240–247 (2002).
[21]C. Scullion, D. Doria, L. Romagnani, A. Sgattoni, K. Naughton, D. R. Symes, P. McKenna, A. Macchi, M. Zepf, S. Kar, and M. Borghesi, "Polarization dependence of bulk ion acceleration from ultrathin foils irradiated by high-intensity ultrashort laser pulses," Phys. Rev. Lett. **119**, 054801 (2017).
[22]A. I. Akhiezer and R. Polovin, "Theory of wave motion of an electron plasma," Z. Eksp. Teor. Fiz. **30**, 915 (1956), http://www.jetp.ac.ru/cgi-bin/dn/e_003_05_0696.pdf.
[23]P. Kaw and J. Dawson, "Relativistic nonlinear propagation of laser beams in cold over dense plasmas," Phys. Fluids **13**, 472 (1970).
[24]C. Max and F. Perkins, "Strong electromagnetic waves in overdense plasmas," Phys. Rev. Lett. **27**, 1342 (1971).
[25]H. W. Powell, M. King, R. J. Gray, D. A. MacLellan, B. Gonzalez-Izquierdo, L. C. Stockhausen, G. Hicks, N. P. Dover, D. R. Rusby, D. C. Carroll, H. Padda, R. Torres, S. Kar, R. J. Clarke, I. O. Musgrave, Z. Najmudin, M. Borghesi, D. Neely, and P. McKenna, "Proton acceleration enhanced by a plasma jet in expanding foils undergoing relativistic transparency," New J. Phys. **17**(10), 103033 (2015).
[26]A. Higginson, R. J. Gray, M. King, R. J. Dance, S. D. R. Williamson, N. M. H. Butler, R. Wilson, R. Capdessus, C. Armstrong, J. S. Green, S. J. Hawkes, P. Martin, W. Q. Wei, S. R. Mirfayzi, X. H. Yuan, S. Kar, M. Borghesi, R. J. Clarke, D. Neely, and P. McKenna, "Near-100 MeV protons via a laser-driven transparency-enhanced hybrid acceleration scheme," Nat. Commun. **9**(1), 724 (2018).
[27]C. S. Brady and T. D. Arber, "An ion acceleration mechanism in laser illuminated targets with internal electron density structure," Plasma Phys. Controlled Fusion **53**(1), 015001 (2011).
[28]T. D. Arber, K. Bennett, C. S. Brady, A. Lawrence-Douglas, M. G. Ramsay, N. J. Sircombe, P. Gillies, R. G. Evans, H. Schmitz, A. R. Bell, and C. P. Ridgers, "Contemporary particle-in-cell approach to laser-plasma modelling," Plasma Phys. Controlled Fusion **57**(11), 113001 (2015).
[29]T. Tajima and J. M. Dawson, "Laser electron accelerator," Phys. Rev. Lett. **43**, 267–270 (1979).
[30]E. Esarey, C. B. Schroeder, and W. P. Leemans, "Physics of laser-driven plasma-based electron accelerators," Rev. Mod. Phys. **81**, 1229–1285 (2009).
[31]W. P. Leemans and E. Esarey, "Summary report: Working group 2 on "Plasma based acceleration concepts"," AIP Conf. Proc. **472**(1), 174 (1999).
[32]J. M. Cole, K. T. Behm, E. Gerstmayr, T. G. Blackburn, J. C. Wood, C. D. Baird, M. J. Duff, C. Harvey, A. Ilderton, A. S. Joglekar, K. Krushelnick, S. Kuschel, M. Marklund, P. McKenna, C. D. Murphy, K. Poder, C. P. Ridgers, G. M. Samarin, G. Sarri, D. R. Symes, A. G. R. Thomas, J. Warwick, M. Zepf, Z. Najmudin, and S. P. D. Mangles, "Experimental evidence of radiation reaction in the collision of a high-intensity laser pulse with a laser-wakefield accelerated electron beam," Phys. Rev. X **8**, 011020 (2018).
[33]S. F. Martins, R. A. Fonseca, W. Lu, W. B. Mori, and L. O. Silva, "Exploring laser-wakefield-accelerator regimes for near-term lasers using particle-in-cell simulation in Lorentz-boosted frames," Nat. Phys. **6**, 311–316 (2010).
[34]K. V. Lezhnin, P. V. Sasorov, G. Korn, and S. V. Bulanov, "High power gamma flare generation in multi-petawatt laser interaction with tailored targets," Phys. Plasmas **25**(12), 123105 (2018).
[35]Y.-J. Gu, M. Jirka, O. Klimo, and S. Weber, "Gamma photons and electron-positron pairs from ultra-intense laser-matter interaction: A comparative study of proposed configurations," Matter Radiat. Extremes **4**(6), 064403 (2019).
[36]T. Nakamura, J. K. Koga, T. Z. Esirkepov, M. Kando, G. Korn, and S. V. Bulanov, "High-power γ-ray flash generation in ultraintense laser-plasma interactions," Phys. Rev. Lett. **108**, 195001 (2012).
[37]R. Capdessus, E. d'Humières, and V. T. Tikhonchuk, "Influence of ion mass on laser-energy absorption and synchrotron radiation at ultrahigh laser intensities," Phys. Rev. Lett. **110**, 215003 (2013).
[38]A. Ferrari, P. Sala, A. Fasso, and J. Ranft, FLUKA: A multi-particle transport code, CERN-2005-10, INFN/TC_05/11, SLAC-R-773.
[39]P. Raczka, J.-L. Dubois, S. Hulin, V. Tikhonchuk, M. Rosiński, A. Zaraś-Szydłowska, and J. Badziak, "Strong electromagnetic pulses generated in high-intensity short-pulse laser interactions with thin foil targets," Laser Part. Beams **35**(4), 677–686 (2017).
[40]M. Mead, "EMP shielding and damage mitigation," IFIN-HH Document No. 1999/03.05.2012.
[41]H. Chen, A. J. Link, R. van Maren, P. K. Patel, R. Shepherd, S. C. Wilks, and P. Beiersdorfer, "High performance compact magnetic spectrometers for energetic ion and electron measurement in ultraintense short pulse laser solid interactions," Rev. Sci. Instrum. **79**(10), 10E533 (2008).
[42]S. Agostinelli, J. Allison, K. Amako, J. Apostolakis, H. Araujo, P. Arce, M. Asai, D. Axen, S. Banerjee, G. Barrand, F. Behner, L. Bellagamba, J. Boudreau, L. Broglia, A. Brunengo, H. Burkhardt, S. Chauvie, J. Chuma, R. Chytracek, G. Cooperman, G. Cosmo, P. Degtyarenko, A. Dell'Acqua, G. Depaola, D. Dietrich, R. Enami, A. Feliciello, C. Ferguson, H. Fesefeldt, G. Folger, F. Foppiano, A. Forti, S. Garelli, S. Giani, R. Giannitrapani, D. Gibin, J. G. Cadenas, I. González, G. G. Abril, G. Greeniaus, W. Greiner, V. Grichine, A. Grossheim, S. Guatelli, P. Gumplinger, R. Hamatsu, K. Hashimoto, H. Hasui, A. Heikkinen, A. Howard, V. Ivanchenko, A. Johnson, F. Jones, J. Kallenbach, N. Kanaya, M. Kawabata, Y. Kawabata, M. Kawaguti, S. Kelner, P. Kent, A. Kimura, T. Kodama, R. Kokoulin, M. Kossov, H. Kurashige, E. Lamanna, T. Lampén, V. Lara, V. Lefebure, F. Lei, M. Liendl, W. Lockman, F. Longo, S. Magni, M. Maire, E. Medernach, K. Minamimoto, P. M. de Freitas, Y. Morita, K. Murakami, M. Nagamatu, R. Nartallo, P. Nieminen, T. Nishimura, K. Ohtsubo, M. Okamura, S. O'Neale, Y. Oohata, K. Paech, J. Perl, A. Pfeiffer, M. Pia, F. Ranjard, A. Rybin, S. Sadilov, E. D. Salvo, G. Santin, T. Sasaki, N. Savvas, Y. Sawada, S. Scherer, S. Sei, V. Sirotenko, D. Smith, N. Starkov, H. Stoecker, J. Sulkimo, M. Takahata, S. Tanaka, E. Tcherniaev, E. S. Tehrani, M. Tropeano, P. Truscott, H. Uno, L. Urban, P. Urban, M. Verderi, A. Walkden, W. Wander, H. Weber, J. Wellisch, T. Wenaus, D. Williams, D. Wright, T. Yamada, H. Yoshida, and D. Zschiesche, "Geant4—A simulation toolkit," Nucl. Instrum. Methods Phys. Res. Sect. A **506**(3), 250–303 (2003).
[43]D. A. Dahl, "Simion for the personal computer in reflection," Int. J. Mass Spectrom. **200**, 3–25 (2000).
[44]R. Weber, J. E. Balmer, and P. Lädrach, "Thomson parabola time-of-flight ion spectrometer," Rev. Sci. Instrum. **57**(7), 1251–1253 (1986).
[45]R. Prasad, D. Doria, S. Ter-Avetisyan, P. S. Foster, K. E. Quinn, L. Romagnani, C. M. Brenner, J. S. Green, P. Gallegos, M. J. V. Streeter, D. C. Carroll, O. Tresca, N. Dover, C. A. J. Palmer, J. Schreiber, D. Neely, Z. Najmudin, and P. McKenna, "Calibration of Thomson parabola—MCP assembly for multi-MeV ion spectroscopy," Nucl. Instrum. Methods Phys. Res., Sect. A **623**(2), 712–715 (2010).
[46]A. Alejo, D. Gwynne, D. Doria, H. Ahmed, D. Carroll, R. Clarke, D. Neely, G. Scott, M. Borghesi, and S. Kar, "Recent developments in the Thomson parabola spectrometer diagnostic for laser-driven multi-species ion sources," J. Instrum. **11**, C10005 (2016).
[47]X. Ribeyre, E. d'Humières, O. Jansen, S. Jequier, V. T. Tikhonchuk, and M. Lobet, "Pair creation in collision of γ-ray beams produced with high-intensity lasers," Phys. Rev. E **93**, 013201 (2016).
[48]G. Glenn, G. Tiwari, G. Dyer, C. Curry, M. Donovan, E. Gaul, M. Gauthier, S. Glenzer, J. Gordon, B. Hegelich, M. Martinez, E. McCary, M. Spinks, and T. Ditmire, "Improved large-energy-range magnetic electron-positron spectrometer for experiments with the Texas Petawatt Laser," J. Instrum. **14**(03), P03012 (2019).

[49]S. Singh, R. Versaci, A. Laso Garcia, L. Morejon, A. Ferrari, M. Molodtsova, R. Schwengner, D. Kumar, and T. Cowan, "Compact high energy x-ray spectrometer based on forward Compton scattering for high intensity laser plasma experiments," Rev. Sci. Instrum. **89**(8), 085118 (2018).

[50]D. Haden, G. Golovin, W. Yan, C. Fruhling, P. Zhang, B. Zhao, S. Banerjee, and D. Umstadter, "High energy x-ray Compton spectroscopy via iterative reconstruction," Nucl. Instrum. Methods Phys. Res., Sect. A **951**, 163032 (2020).

[51]Y. Rhee, S. Nam, J. Peebles, H. Sawada, M. Wei, X. Vaisseau, T. Sasaki, L. Giuffrida, S. Hulin, B. Vauzour, J. Santos, D. Batani, H. Mclean, P. Patel, Y. Li, D. Yuan, K. Zhang, J. Zhong, C. Fu, and C. Nam, "Spectral tomographic analysis of bremsstrahlung X-rays generated in a laser-produced plasma," Laser Part. Beams **34**, 645–654 (2016).

[52]D. R. Rusby, C. D. Armstrong, C. M. Brenner, R. J. Clarke, P. McKenna, and D. Neely, "Novel scintillator-based x-ray spectrometer for use on high repetition laser plasma interaction experiments," Rev. Sci. Instrum. **89**(7), 073502 (2018).

[53]J. Allison *et al.*, "Recent developments in Geant4," Nucl. Instrum. Methods Phys. Res., Sect. A **835**, 186–225 (2016).

[54]R. Brun and F. Rademakers, "Root: An object oriented data analysis framework," Nucl. Instrum. Methods Phys. Res., Sect. A **A389**, 81–86 (1997).

[55]W. P. Leemans, A. J. Gonsalves, H.-S. Mao, K. Nakamura, C. Benedetti, C. B. Schroeder, C. Tóth, J. Daniels, D. E. Mittelberger, S. S. Bulanov, J.-L. Vay, C. G. R. Geddes, and E. Esarey, "Multi-GeV electron beams from capillary-discharge-guided subpetawatt laser pulses in the self-trapping regime," Phys. Rev. Lett. **113**, 245002 (2014).

[56]M. Vargas, W. Schumaker, Z.-H. He, Z. Zhao, K. Behm, V. Chvykov, B. Hou, K. Krushelnick, A. Maksimchuk, V. Yanovsky, and A. Thomas, "Improvements to laser wakefield accelerated electron beam stability, divergence, and energy spread using three-dimensional printed two-stage gas cell targets," Appl. Phys. Lett. **104**(17), 174103 (2014).

[57]G. M. Samarin, M. Zepf, and G. Sarri, "Radiation reaction studies in an all-optical set-up: Experimental limitations," J. Mod. Opt. **65**(11), 1362–1369 (2018).

[58]K. M. Spohr, M. Shaw, W. Galster, K. W. D. Ledingham, L. Robson, J. M. Yang, P. McKenna, T. McCanny, J. J. Melone, K.-U. Amthor, F. Ewald, B. Liesfeld, H. Schwoerer, and R. Sauerbrey, "Study of photo-proton reactions driven by bremsstrahlung radiation of high-intensity laser generated electrons," New J. Phys. **10**(4), 043037 (2008).

[59]J. F. Ziegler, "SRIM-2003," Nucl. Instrum. Methods Phys. Res., Sect. B **219-220**, 1027–1036 (2004), Proceedings of the Sixteenth International Conference on Ion Beam Analysis.

[60]A. Cucoanes, M. Gugiu, F. Rotaru, F. Negoita, L. Tudor, S. Kisyov, C. Manailescu, and V. Nastasa, "Radiochromic film calibration at 9 MV accelerator of IFIN-HH," Romanian Acad. A **20**(1), 29–36 (2019).

[61]D. L. Balabanski, R. Popescu, D. Stutman, K. A. Tanaka, O. Tesileanu, C. A. Ur, D. Ursescu, and N. V. Zamfir, "New light in nuclear physics: The extreme light infrastructure," EPL (Europhys. Lett.) **117**(2), 28001 (2017).

[62]D. Filipescu, A. Anzalone, D. L. Balabanski, S. S. Belyshev, F. Camera, M. La Cognata, P. Constantin, L. Csige, P. V. Cuong, M. Cwiok, V. Derya, W. Dominik, M. Gai, S. Gales, I. Gheorghe, B. S. Ishkhanov, A. Krasznahorkay, A. A. Kuznetsov, C. Mazzocchi, V. N. Orlin, N. Pietralla, M. Sin, C. Spitaleri, K. A. Stopani, O. Tesileanu, C. A. Ur, I. Ursu, H. Utsunomiya, V. V. Varlamov, H. R. Weller, N. V. Zamfir, and A. Zilges, "Perspectives for photonuclear research at the Extreme Light Infrastructure-nuclear physics (ELI-NP) facility," Eur. Phys. J. A **51**(12), 185 (2015).

[63]U. Kneissl and A. Zilges, "The nuclear resonance fluorescence method," in *Landolt-Börnstein: Group I: Elementary Particles, Nuclei and Atoms* (Springer-Verlag, Berlin, Heidelberg, 2012), Vol. 25B, pp. 30–47.

[64]C. A. Ur, A. Zilges, N. Pietralla, J. Beller, B. Boisdeffre, M. Cernaianu, V. Derya, B. Loeher, C. Matei, G. Pascovici, C. Petcu, C. Romig, D. Savarn, G. Suliman, E. Udup, and V. Werner, "Nuclear resonance fluorescence experiments at ELI-NP," Rom. Rep. Phys. **68**, S483–S538 (2016).

[65]H. Scraggs, C. Pearson, G. Hackman, M. Smith, R. Austin, G. Ball, A. Boston, P. Bricault, R. Chakrawarthy, R. Churchman, N. Cowan, G. Cronkhite, E. Cunningham, T. Drake, P. Finlay, P. Garrett, G. Grinyer, B. Hyland, B. Jones, J. Leslie, J.-P. Martin, D. Morris, A. Morton, A. Phillips, F. Sarazin, M. Schumaker, C. Svensson, J. Valiente-Dobon, J. Waddington, L. Watters, and L. Zimmerman, "TIGRESS highly-segmented high-purity germanium clover detector," Nucl. Instrum. Methods Phys. Res., Sect. A **543**, 431–440 (2005).

[66]P.-G. Reinhard and W. Nazarewicz, "Information content of a new observable: The case of the nuclear neutron skin," Phys. Rev. C **81**, 051303 (2010).

[67]K. M. Spohr, K. Ledingham, R. Chapman, M. Hassan, J. Melone, S. Pain, and J. Smith, "Precision measurement of the dipole polarizability α_D of ^{208}Pb with high intensity, monoenergetic MeV γ radiation for the evaluation of neutron skin and the enhancement of UNEDF theory," in *The White Book of ELI Nuclear Physics, ELI-NP/IFIN-HH*, edited by J. Chambaret, R. Dabu, and D. Ursescu (■, 2010), Chap. 5, pp. 92–94.

[68]J. Piekarewicz, "Pygmy resonances and neutron skins," Phys. Rev. C **83**, 034319 (2011).

[69]X. Roca-Maza, M. Brenna, G. Colò, M. Centelles, X. Viñas, B. K. Agrawal, N. Paar, D. Vretenar, and J. Piekarewicz, "Electric dipole polarizability in ^{208}Pb: Insights from the droplet model," Phys. Rev. C **88**, 024316 (2013).

[70]O. Bohigas, N. Van Giai, and D. Vautherin, "Selfconsistent description of the static nuclear dipole polarizability," Phys. Lett. B **102**, 105–108 (1981).

[71]T. Hashimoto, A. M. Krumbholz, P.-G. Reinhard, A. Tamii, P. von Neumann-Cosel, T. Adachi, N. Aoi, C. A. Bertulani, H. Fujita, Y. Fujita, E. Ganioğlu, K. Hatanaka, E. Ideguchi, C. Iwamoto, T. Kawabata, N. T. Khai, A. Krugmann, D. Martin, H. Matsubara, K. Miki, R. Neveling, H. Okamura, H. J. Ong, I. Poltoratska, V. Yu. Ponomarev, A. Richter, H. Sakaguchi, Y. Shimbara, Y. Shimizu, J. Simonis, F. D. Smit, G. Süsoy, T. Suzuki, J. H. Thies, M. Yosoi, and J. Zenihiro, "Dipole polarizability of ^{120}Sn and nuclear energy density functionals," Phys. Rev. C **92**, 031305 (2015).

[72]A. Tamii, I. Poltoratska, P. von Neumann-Cosel, Y. Fujita, T. Adachi, C. A. Bertulani, J. Carter, M. Dozono, H. Fujita, K. Fujita, K. Hatanaka, D. Ishikawa, M. Itoh, T. Kawabata, Y. Kalmykov, A. M. Krumbholz, E. Litvinova, H. Matsubara, K. Nakanishi, R. Neveling, H. Okamura, H. J. Ong, B. Özel-Tashenov, V. Y. Ponomarev, A. Richter, B. Rubio, H. Sakaguchi, Y. Sakemi, Y. Sasamoto, Y. Shimbara, Y. Shimizu, F. D. Smit, T. Suzuki, Y. Tameshige, J. Wambach, R. Yamada, M. Yosoi, and J. Zenihiro, "Complete electric dipole response and the neutron skin in ^{208}Pb," Phys. Rev. Lett. **107**, 062502 (2011).

[73]F. Camera, H. Utsunomiya, D. Varlamov, D. Filipescu, V. Baran, A. Bracco, G. Colò, I. Gheorghe, T. Glodariu, C. Matei, and O. Wieland, "Gamma above the neutron threshold experiments at ELI-NP," Rom. Rep. Phys. **68**, S539–S619 (2016).

[74]M. Krzysiek, F. Camera, D. Filipescu, H. Utsunomiya, G. Colò, I. Gheorghe, and Y. Niu, "Simulation of the ELIGANT-GN array performances at ELI-NP for gamma beam energies larger than neutron threshold," Nucl. Instrum. Methods Phys. Res., Sect. A **916**, 257–274 (2019).

[75]M. Krzysiek, H. Utsunomiya, I. Gheorghe, D. Filipescu, T. Renstrom, G. Tveten, S. Belyshev, K. Stopani, H. Wang, G. Fan, Y. Lui, D. Symochko, S. Goriely, A. Larsen, S. Siem, V. Varlamov, B. Ishkhanov, T. Ari-izumi, and S. Miyamoto, "Photoneutron cross-section measurements for ^{165}Ho by the direct neutron-multiplicity sorting technique at NewSUBARU," Acta Phys. Pol. B **50**(3), 487–494 (2018).

[76]B. L. Berman and S. C. Fultz, "Measurements of the giant dipole resonance with monoenergetic photons," Rev. Mod. Phys. **47**, 713–761 (1975).

[77]H. Utsunomiya, Y. Yonezawa, H. Akimune, T. Yamagata, M. Ohta, M. Fujishiro, H. Toyokawa, and H. Ohgaki, "Photodisintegration of ^{9}Be with laser-induced Compton backscattered γ rays," Phys. Rev. C **63**, 018801 (2000).

[78]C. W. Arnold, T. B. Clegg, C. Iliadis, H. J. Karwowski, G. C. Rich, J. R. Tompkins, and C. R. Howell, "Cross-section measurement of ^{9}Be$(\gamma, n)^{8}$Be and implications for $\alpha + \alpha + n \rightarrow {}^{9}$Be in the r process," Phys. Rev. C **85**, 044605 (2012).

[79]H. Utsunomiya, S. Katayama, I. Gheorghe, S. Imai, H. Yamaguchi, D. Kahl, Y. Sakaguchi, T. Shima, K. Takahisa, and S. Miyamoto, "Photodisintegration of ^{9}Be through the $1/2^{+}$ state and cluster dipole resonance," Phys. Rev. C **92**, 064323 (2015).

[80]D. Balabanski, F. Ibrahim, A. Krasnahorkay, I. Boztosun, D. Choudhury, S. Coban, P. Constantin, L. Csige, P. Cuong, T. Dickel, H. Djapo, I. Dobrin, S. Essabaa, D. Filipescu, S. Franchoo, G. Georgiev, I. Gheorghe, D. G. Ghita, T. Glodariu, M. Gupta, A. Jokinen, J. Kaur, N. Marginean, R. Marginean, I. Moore, H. Pentilla, C. Petcu, P. Plass, T. Sava, G. Savard, C. Scheidenberger, and D. Yordanov, "Photofission experiments at ELI-NP," Rom. Rep. Phys. **68**, S621–S698 (2016).

[81]O. Tesileanu, M. Gai, M. Anzalone, C. Balan, J. Bihalowicz, M. Cwiok, W. Dominik, S. Gales, D. G. Ghita, Z. Janos, D. Kendellen, M. La Cognata, C. Matei, K. Mikszuta, C. Petcu, M. Pfützner, T. Matulewicz, C. Mazzocchi, and C. Spitaleri, "Charged particle detection at ELI-NP," Rom. Rep. Phys. **68**, S699–S734 (2016).

[82]A. Krasznahorkay, "Tunnelling through triple-humped fission barriers," in *Handbook of Nuclear Chemistry*, edited by A. Vertes (Springer, New York, 2011), pp. 281–318.

[83]M. Cwiok, M. Bieda, J. Bihalowicz, Z. Dominik, W. Janas, L. Janiak, J. Mańczak, T. Matulewicz, C. Mazzocchi, M. Pfützner, P. Podlaski, S. Sharma, M. Zaremba, D. L. Balabanski, A. Bey, D. G. Ghita, O. Tesileanu, and M. Gai, "A TPC detector for studying photo-nuclear reactions at astrophysical energies with gamma-ray beams at ELI–NP," Acta Phys. Pol. B **49**, 509–514 (2018).
[84]M. Gai, D. Schweitzer, S. R. Stern, A. H. Young, R. Smith, M. Cwiok, J. S. Bihalowicz, H. Czyrkowski, R. Dabrowski, W. Dominik, A. Fijalkowska, Z. Janas, L. Janiak, A. Korgul, T. Matulewicz, C. Mazzocchi, M. Pfützner, M. Zaremba, D. Balabanski, I. Gheorghe, C. Matei, O. Tesileanu, N. V. Zamfir, M. W. Ahmed, S. S. Henshaw, C. R. Howell, J. M. Mueller, L. S. Myers, S. Stave, C. Sun, H. R. Weller, Y. K. Wu, A. Breskin, V. Dangendorf, K. Tittelmeier, and M. Freer, "Time Projection Chamber (TPC) detectors for nuclear astrophysics studies with gamma beams," Nucl. Instrum. Methods Phys. Res., Sect. A **954**, 161779 (2020).
[85]D. Savran, T. Aumann, and A. Zilges, "Experimental studies of the pygmy dipole resonance," Prog. Part. Nucl. Phys. **70**, 210 (2013).
[86]N. Tsoneva and H. Lenske, "Pygmy quadrupole resonance in skin nuclei," Phys. Lett. B **695**, 174 (2011).
[87]L. Pellegri, A. Bracco, N. Tsoneva, R. Avigo, G. Benzoni, N. Blasi, S. Bottoni, F. Camera, S. Ceruti, F. C. L. Crespi, A. Giaz, S. Leoni, H. Lenske, B. Million, A. I. Morales, R. Nicolini, O. Wieland, D. Bazzacco, P. Bednarczyk, B. Birkenbach, M. Ciemała, G. de Angelis, E. Farnea, A. Gadea, A. Görgen, A. Gottardo, J. Grebosz, R. Isocrate, M. Kmiecik, M. Krzysiek, S. Lunardi, A. Maj, K. Mazurek, D. Mengoni, C. Michelagnoli, D. R. Napoli, F. Recchia, B. Siebeck, S. Siem, C. A. Ur, and J. J. Valiente-Dobón, "Multitude of 2^+ discrete states in ^{124}Sn observed via the (^{17}O, ^{17}O$'\gamma$) reaction: Evidence for pygmy quadrupole states," Phys. Rev. C **92**, 014330 (2015).
[88]M. Spieker, N. Tsoneva, V. Derya, D. S. J. Endres, P. Butler, M. N. Harakeh, S. Harissopulos, R.-D. Herzberg, R. Krücken, A. Lagoyannis, H. Lenske, N. Pietralla, L. Popescu, M. Scheck, F. Schlüter, V. S. K. Sonnabend, H. Wörtche, and A. Zilges, "The pygmy quadrupole resonance and neutron-skin modes in ^{124}Sn," Phys. Lett. B **752**, 102–107 (2016).
[89]N. Tsoneva, H. Lenske, and C. Stoyanov, "Probing the nuclear neutron skin by low-energy dipole modes," Phys. Lett. B **586**, 213 (2004).
[90]N. Tsoneva and H. Lenske, "Pygmy dipole resonances in the tin region," Phys. Rev. C **77**, 024321 (2008).
[91]A. Bracco, F. C. L. Crespi, and E. G. Lanza, "Gamma decay of pygmy states from inelastic scattering of ions," Eur. Phys. J. A **51**(8), 99 (2015).
[92]N. Paar, D. Vretenar, E. Khan, and G. Colò, "Exotic modes of excitation in atomic nuclei far from stability," Rep. Prog. Phys. **70**(5), 691–793 (2007).
[93]N. Tsoneva and H. Lenske, "Energy–density functional plus quasiparticle–phonon model theory as a powerful tool for nuclear structure and astrophysics," Phys. At. Nucl. **79**(6), 885–903 (2016).
[94]V. G. Soloviev, *Theory of Complex Nuclei* (Pergamon Press, Oxford, 1976).
[95]M. Grinberg and C. Stoyanov, "Distribution of two-phonon strength in even N = 82 nuclei," Nucl. Phys. A **573**, 231 (1994).
[96]V. Ponomarev, C. Stoyanov, N. Tsoneva, and M. Grinberg, "Boson forbidden low-energy E1-transitions in spherical nuclei," Nucl. Phys. A **635**(4), 470–483 (1998).
[97]A. Tonchev, N. Tsoneva, C. Bhatia, C. Arnold, S. Goriely, S. Hammond, J. Kelley, E. Kwan, H. Lenske, J. Piekarewicz, R. Raut, G. Rusev, T. Shizuma, and W. Tornow, "Pygmy and core polarization dipole modes in ^{206}Pb: Connecting nuclear structure to stellar nucleosynthesis," Phys. Lett. B **773**, 20 (2017).
[98]N. Tsoneva, M. Spieker, H. Lenske, and A. Zilges, "Fine structure of the pygmy quadrupole resonance in ^{112,114}Sn," Nucl. Phys. A **990**, 183–198 (2019).
[99]R. Raut, A. P. Tonchev, G. Rusev, W. Tornow, C. Iliadis, M. Lugaro, J. Buntain, S. Goriely, J. H. Kelley, R. Schwengner, A. Banu, and N. Tsoneva, Cross-section measurements of the ^{86}Kr(γ, n) reaction to probe the *s*-process branching at ^{85}Kr, Phys. Rev. Lett. **111**, 112501 (2013).
[100]N. Tsoneva, S. Goriely, H. Lenske, and R. Schwengner, "Pygmy resonances and radiative nucleon captures for stellar nucleosynthesis," Phys. Rev. C **91**, 044318 (2015).
[101]G. Priebe, D. Laundy, M. Macdonald, G. Diakun, S. Jamison, L. Jones, D. Holder, S. Smith, P. Phillips, B. Fell, B. Sheehy, N. Naumova, I. Sokolov, S. Ter-Avetisyan, K. M. Spohr, G. A. Krafft, J. B. Rosenzweig, U. Schramm, F. Grüner, G. J. Hirst, J. Collier, S. Chattopadhyay, and E. A. Seddon, "Inverse Compton backscattering source driven by the multi-10 TW laser installed at Daresbury," Laser Part Beams **26**(4), 649–660 (2008).
[102]G. Priebe, D. Filippetto, O. Williams, Y. M. Saveliev, L. B. Jones, D. Laundy, M. A. MacDonald, G. P. Diakun, P. J. Phillips, S. P. Jamison, K. M. Spohr, S. Ter-Avetisyan, G. J. Hirst, J. Collier, E. A. Seddon, and S. L. Smith, "Status of the inverse Compton backscattering source at Daresbury laboratory," Nucl. Instrum. Methods Phys. Res., Sect. A **608**, S109–S112 (2009).
[103]S. P. D. Mangles, C. D. Murphy, Z. Najmudin, A. G. R. Thomas, J. L. Collier, A. E. Dangor, E. J. Divall, P. S. Foster, J. G. Gallacher, C. J. Hooker, D. A. Jaroszynski, A. J. Langley, W. B. Mori, P. A. Norreys, F. S. Tsung, R. Viskup, B. R. Walton, and K. Krushelnick, "Monoenergetic beams of relativistic electrons from intense laser–plasma interactions," Nature **431**, 535–538 (2004).
[104]C. G. R. Geddes, C. Toth, J. van Tilborg, E. Esarey, C. B. Schroeder, D. Bruhwiler, C. Nieter, J. Cary, and W. P. Leemans, "High-quality electron beams from a laser wakefield accelerator using plasma-channel guiding," Nature **431**, 538–541 (2004).
[105]J. Faure, Y. Glinec, A. Pukhov, S. Kiselev, S. Gordienko, E. Lefebvre, J. P. Rousseau, F. Burgy, and V. Malka, "A laser–plasma accelerator producing monoenergetic electron beams," Nature **431**, 541–544 (2004).
[106]W. P. Leemans, B. Nagler, A. J. Gonsalves, C. Tóth, K. Nakamura, C. G. R. Geddes, E. Esarey, C. B. Schroeder, and S. M. Hooker, "GeV electron beams from a centimetre-scale accelerator," Nat. Phys. **2**, 696–699 (2006).
[107]K. Homma, O. Tesileanu, L. D'Alessi, T. Hasebe, A. Ilderton, T. Moritaka, Y. Nakamiya, K. Seto, H. Utsunomiya, and Y. Xu, "Combined laser gamma experiment at ELI-NP," Rom. Rep. Phys. **68**, S233 (2016).
[108]H. Ejiri, T. Shima, S. Miyamoto, K. Horikawa, Y. Kitagawa, Y. Asano, S. Daté, and Y. Ohashi, "Resonant photonuclear reactions for isotope transmutation," J. Phys. Soc. Jpn. **80**(9), 094202 (2011).
[109]H. Ejiri and T. Shima, "Resonant photonuclear isotope detection using medium-energy photon beam," Phys. Rev. Spec. Top.–Accel. Beams **15**, 024701 (2012).
[110]S. M. Seltzer and M. J. Berger, "Bremsstrahlung spectra from electron interactions with screened atomic nuclei and orbital electrons," Nucl. Instrum. Methods Phys. Res., Sect. B **12**(1), 95–134 (1985).
[111]K. Ta Phuoc, S. Corde, C. Thaury, V. Malka, A. Tafzi, J. P. Goddet, R. C. Shah, S. Sebban, and A. Rousse, "All-optical Compton gamma-ray source," Nat. Photonics **6**, 308–311 (2012).
[112]C. Yu, R. Qi, W. Wang, J. Liu, W. Li, C. Wang, Z. Zhang, J. Liu, Z. Qin, M. Fang, K. Feng, Y. Wu, Y. Tian, Y. Xu, F. Wu, Y. Leng, X. Weng, J. Wang, F. Wei, Y. Yi, Z. Song, R. Li, and Z. Xu, "Ultrahigh brilliance quasi-monochromatic MeV γ-rays based on self-synchronized all-optical Compton scattering," Sci. Rep. **6**, 29518 (2016).
[113]H.-E. Tsai, X. Wang, J. M. Shaw, Z. Li, A. V. Arefiev, X. Zhang, R. Zgadzaj, W. Henderson, V. Khudik, G. Shvets, and M. C. Downer, "Compact tunable Compton X-ray source from laser-plasma accelerator and plasma mirror," Phys. Plasmas **22**(2), 023106 (2015).
[114]H.-E. Tsai, A. V. Arefiev, J. M. Shaw, D. J. Stark, X. Wang, R. Zgadzaj, and M. C. Downer, "Self-aligning concave relativistic plasma mirror with adjustable focus," Phys. Plasmas **24**(1), 013106 (2017).
[115]J. F. Ong, W. R. Teo, T. Moritaka, and H. Takabe, "Radiation reaction in the interaction of ultraintense laser with matter and gamma-ray source," Phys. Plasmas **23**(5), 053117 (2016).
[116]J. F. Ong, T. Moritaka, and H. Takabe, "The suppression of radiation reaction and laser field depletion in laser-electron beam interaction," Phys. Plasmas **25**(3), 033113 (2018).
[117]J. F. Ong, K. Seto, A. C. Berceanu, S. Aogaki, and L. Neagu, "Feasibility studies of an all-optical and compact γ-ray blaster using a 1 PW laser pulse," Plasma Phys. Controlled Fusion **61**(8), 084009 (2019).
[118]S. Ataman, M. Cuciuc, L. D'Alessi, L. Neagu, M. Rosu, K. Seto, O. Tesileanu, Y. Xu, and M. Zeng, "Experiments with combined laser and gamma beams at ELI-NP," AIP Conf. Proc. **1852**(1), 070002 (2017).
[119]K. Homma and Y. Nakamiya, "Gamma Polari-calorimetry with SOI pixels for proposals at extreme light infrastructure (ELI-NP)," in Proceedings of the International Workshop on SOI Pixel Detector (SOIPIX2015), Sendai, Miyagi, Japan, 03–06 June 2015; arXiv:1507.06179.
[120]C. de Jager, B. Wojtsekhowski, D. Tedeschi, B. Vlahovic, D. Abbott, J. Asai, G. Feldman, T. Hotta, M. Khadaker, H. Kohri, T. Matsumara, T. Mibe, T. Nakano, V. Nelyubin, G. Orielly, A. Rudge, P. Weilhammer, M. Wood, T. Yorita, and R. Zegers, "A pair polarimeter for linearly polarized high energy photons," Eur. Phys. J. A **19**(1), 275–278 (2004).